Advances in Science and Technology
Research Journal

Advances in Science and Technology Research Journal, 2026, 20(7), 352–377
https://doi.org/10.12913/22998624/219086
ISSN 2299-8624, License CC-BY 4.0

Received: 2025.12.19
Accepted: 2026.05.15
Published: 2026.06.01

Dressing of superabrasive profile grinding wheels with a tangential laser beam: A review

Ryszard Dębkowski[1]

[1] Institute of Machine Tools and Production Engineering, Faculty of Mechanical Engineering, Lodz University of Technology, ul. Stefanowskiego 1/15 0, 90-537 Łódź, Poland
E-mail: ryszard.debkowski@p.lodz.pl

ABSTRACT

Superabrasive profile grinding wheels, owing to their high cutting properties and long durability life, are gaining increasingly widespread use and, in many cases, represent the only type of tool capable of ensuring efficient and precise machining of hard and brittle materials employed in modern structures within the optical, electronic, aerospace, and tooling industries. The dressing of profile grinding wheels can be carried out using various methods; however, in contemporary production systems focused on high flexibility and rapid response to market demands, particular importance is placed on solutions that enable easy reconfiguration of the process. These requirements are met by laser-beam dressing. This method can be applied to grinding wheels with various types of bonding and abrasive materials. It enables the formation of arbitrary profiles on the wheel circumference, is characterized by high efficiency, and offers reduced environmental impact. Moreover, the absence of wear of the dressing tool makes the method economically competitive. The paper integrates and systematizes information previously presented in dispersed publications, providing a coherent overview of the current state of knowledge and the development directions of tangential laser-beam dressing technology. The study encompasses both the physical fundamentals of laser processing of grinding wheels and an analysis of research results concerning classical and innovative solutions for dressing superabrasive grinding wheels. Available findings indicate that the highest profile-shaping accuracy is achieved through the integration of a multi-stage laser machining strategy – including roughing and finishing stages – with adaptive compensation of the beam path. Increasing attention is also drawn to the importance of ultrashort pulse laser sources, which enable precise surface shaping while minimizing undesirable material changes. The review highlights the need to develop a universal method that ensures high material removal rates, submicron shaping accuracy, and minimal microstructural changes as well as minimal degradation of the wheel's operational properties. Directions for further research should focus on the development of in-process measurement methods enabling the monitoring of grinding wheel geometry and ablation parameters, integration of monitoring systems with CNC control systems to implement real-time corrections, as well as modeling of energy distribution and coupled thermal-material phenomena in the ablation zone.

Keywords: dressing, superabrasive, profile wheel, grinding, laser machining, laser beam.

INTRODUCTION

Advances in manufacturing techniques are contributing to the increasingly widespread use of hard and brittle materials in many industries (aerospace, defence, communications and electronics), whose properties, such as high resistance to heat, chemicals, high transmission and low optical absorption, high electrical insulation, and wear resistance, are useful in specific applications. These materials include sintered carbides, ceramics, fused silica, precious stones, silicon carbide and crystalline silicon. In many applications, parts made of these materials require very precise machining to ensure high dimensional accuracy and high surface quality. However, their hardness and brittleness make them difficult to machine. One method that can meet these requirements and is also efficient is grinding with superabrasive grinding wheels. These are grinding wheels in which the abrasive is cubic boron nitride (CBN) or synthetic diamond (SD) grains, the bonds these wheels are vitrified, metal, resinoid, electroplated or hybrid. The advantage of these grinding wheels is their high durability (significantly exceeding the durability of conventional grinding wheels with aluminum oxide or silicon carbide as the abrasive), i.e. a long period of maintaining good cutting properties and active surface shape, which enables efficient machining of many workpieces with a repeatable, high-quality surface.

The wear of grinding wheels, which progresses with prolonged use, is a consequence of the physical and chemical phenomena occurring during grinding. As a result, cracking, abrasion, and chipping of abrasive grains occur, the height of their protrusion above the binder is reduced, and the shape of the active surface of the grinding wheel is degraded. Limited cutting capacity prevents the abrasive from penetrating into the workpiece and forming chips. This reduces grinding efficiency, and the increase in friction and grinding forces causes negative changes on the ground surface and vibrations in the machine tool-chuck-workpiece-tool system. It then becomes necessary to perform a procedure to restore the initial condition (centricity, shape, cutting properties) of the grinding wheel active surface – dressing.

This process is difficult to perform due to the high hardness of the abrasive and the need to maintain narrow tolerances (especially in the case of shaped grinding wheels). Traditional mechanical methods involve two stages of dressing. The first stage is to cause the tips of the abrasive grains to break, thereby creating new, sharp edges and the required shape of the grinding wheel. Since after this stage the tips of the abrasive grains do not protrude sufficiently above the binder, a second treatment is necessary. In this stage, the binder is removed in such an amount that sufficient space for chips is created between the abrasive grains, and the abrasive grains are not excessively weakened. The tools used in the first stage are single-point diamond dressers or diamond rolls [1,2]. The second stage involves grinding the superabrasive grinding wheel with a conventional silicon carbide SiC grinding wheel. Mechanical dressing methods are time-consuming and, due to high tool wear, relatively expensive and do not provide sufficient grain protrusion above the binder. In addition, SiC grinding wheel wear products increase the risk of abrasive damage to the grinding machine components. Methods using electric current to initiate bonding material dissolution, such as ELID Electrolytic in-process dressing [3,4], ECD – electro chemical dressing [5], ECCG – electrochemical cleaning grinding [6], EDD – electrical discharge dressing [7,8], WEDD – wire electro discharge dressing [9], ECDD – electro–contact discharge dressing [10–12], EDG – dressing by electrical discharge grinding method [13], are applicable to grinding wheels that conduct electricity, i.e. those with a metal bond or metal-coated abrasive. When deciding to use them, it is necessary to ensure an appropriate power supply, safe power supply to the electrode and grinding wheel, and an electrode with dimensions and shape appropriate for the operation being performed. The disadvantages of methods using electric current include the possibility of uncontrolled, harmful effects on the abrasive, the need to dispose of used working fluid (if used) and difficulties in controlling the size of the gap between the wearing electrode and the grinding wheel. The methods using high-energy AWJ water-abrasive jet to dress superabrasive grinding wheels prove to be inaccurate and can only be used for rough dressing [14,15]. Solutions aimed at limiting the shortcomings of individual methods (mechanical, including AWJ, electrolytic, electroerosion) involve the creation of combined methods. The advantages of one method can then compensate for the disadvantages of another. For example, an accurate grinding wheel profile and the correct protrusion of the grains above the binder were achieved by using the following methods in sequence: rough AWJ profiling, in which the water-abrasive jet is fed tangentially into the gap between the grinding wheel and the diamond roller, which is approximately 0.5 times the size of the abrasive particle; fine touch profiling by grinding a steel block; AWJ sharpening carried out in the same way as rough profiling but with lower water pressure and a greater nozzle distance [16]. Another combined method involves supporting the dressing process performed with a single-grain diamond dressing tool with so-called dry electrical discharges. The discharges are designed to heat and soften the abrasive wheel material immediately before contact with the tip of the dressing tool [17], thus reducing its wear rate.

The development of superabrasive grinding wheel conditioning technology is a constantly evolving issue, particularly due to the increasingly wide range of applications for these grinding wheels. Research is ongoing into methods that will ensure high performance and accuracy, low treatment costs and suitability for a wide range of grinding wheel types and sizes.

Over the last 40 years, significant progress has been made in the development of laser dressing methods. This is due to the increasing availability of laser equipment and advances in its design. The emergence of new types of lasers (fibre, solid-state) has made it possible to easily deliver and direct the laser beam to the treatment site, while pulsed lasers with very short pulses (e.g. picosecond) have reduced the impact of thermodynamic phenomena on the condition of the material in the laser ablation zone. Laser dressing has many advantages, including high efficiency and no mechanical interaction between the tool and the workpiece, which means that the dressing tool is not subject to wear and the workpiece is not subject to deflection and vibration. Laser beam dressing is a flexible method that allows for the processing of grinding wheels with different geometries and, thanks to the possibility of setting the beam parameters, for the selective ablation of individual components of the grinding wheel. The dressing results are repeatable in subsequent treatments, and the process itself can be automated. Another important aspect of the development of this method is its limited environmental effect.

A specific case of applying laser technology is the dressing of profile grinding wheels. These tools are used to increase the efficiency of the grinding process by directly transferring the contour of the wheel's active surface onto the workpiece surface, thereby eliminating the need for profiling motions performed by the wheel. The use of profile grinding wheels additionally enables the simultaneous machining of multiple surfaces (e.g., concurrent edge chamfering on both sides of a insert), as well as the machining of surfaces with aspherical or free-form geometries. The specificity of dressing profile grinding wheels with a laser beam results from the properties of the beam itself. The beam does not possess a clearly defined active boundary, and its diameter – and thus its power density – varies along the path between the focusing optics and the focal point. This variability constitutes a significant limitation to precisely reproducing the designed profile on the wheel surface, making the process more complex compared to mechanical conditioning techniques. Research results concerning laser conditioning of profiled grinding wheels are available in the international literature; however, existing review papers on conditioning methods [18–21] typically do not treat this issue as a distinct research area. Given the growing relevance and developmental potential of laser technology in the preparation of abrasive tools, this study presents a literature review that aims to synthesise and analyse the current state of the art in the field of profile dressing of grinding wheels using a laser beam.

BASICS OF GRINDING WHEELS LASER TRUING AND DRESSING

Properties of the laser beam

In laser machining, the role of the blade removing the layer of bonding material and abrasive grains is performed by a high-energy beam of electromagnetic radiation concentrated by an optical system (Figure 1). During dressing, the grinding wheel moves at a constant rotational speed, and the beam performs a scanning motion along the generatrix of the grinding wheel. The radiation energy is absorbed by the materials that make up the abrasive layer of the grinding wheel. At the appropriate power density of the incident radiation, phenomena causing material ablation to occur on the surface of the grinding wheel. Figure 1 shows two basic ways of positioning the laser beam relative to the surface of the grinding wheel during dressing, i.e. radial and tangential.

The course of the process and the final effect of laser machining depend on many factors, including: the properties of the laser beam, the kinematic parameters of the operation, direction of incidence of the beam on the grinding wheel surface, the thermal and optical properties of the materials of which the grinding wheel is made, and the position of the focal point of the focused beam relative to the surface of the material being irradiated. Each of the above factors directly or indirectly affects the shape and dimensional accuracy of the grinding wheel after dressing, the topography of its surface, and the physical properties of the grinding wheel materials, which may have changed because of the heat and atmosphere in which the dressing was performed. The beam properties that have a direct impact on the shape and dimensional accuracy of the grinding wheel after dressing are:

- no 'end' of the beam that could be treated as the edge of the blade, as is the case with mechanical tools for dressing grinding wheels,

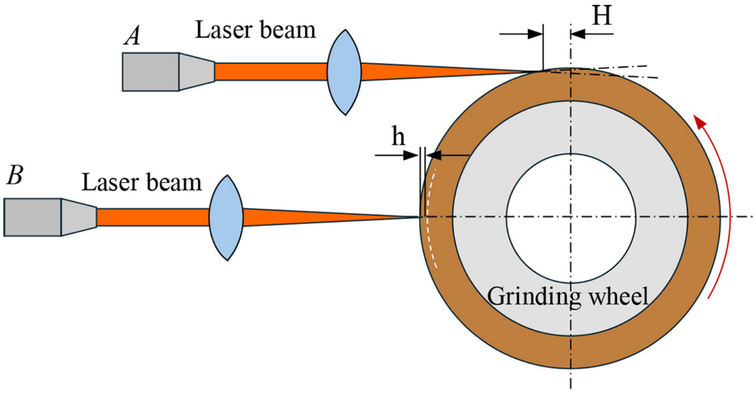

Figure 1. Positioning of the laser beam relative to the grinding wheel during dressing, A – tangential, B – radial

- variable radiation power density with changing distance from the beam focus and within its cross-section,

The “blade” of the laser beam is the spot formed by the beam on the surface of the grinding wheel. The size and shape of the spot depend on the distance between the surface of the grinding wheel and the focal point of the beam, the angle of incidence of the beam on the surface of the grinding wheel, and the shape and topography of the grinding wheel. The smallest spot is created by a beam falling on a smooth surface perpendicular to its axis, located at a distance equal to the focal length of the optical system of the laser head. The spot is then located at the focus of the beam. At this point, the radiation power density is highest. When the irradiated surface is outside the beam focus, defocusing and enlargement of the spot occur. As a result of beam dispersion, the radiation power density in the spot area is lower (Figure 2).

The causes of beam defocusing can be varied. Figure 1 shows the lengths (*h*, *H*) over which beam defocusing can occur, resulting from the movement of the rough grinding wheel surface relative to the beam focal point. For example, when the beam is directed radially and its focal point is at a constant distance from the grinding wheel axis equal to the maximum radius formed by the peaks of the surface roughness profile, as the grinding wheel rotates, a beam with varying power density reaches the valleys of its surface, resulting from defocusing that occurred along a distance corresponding to the current profile height. More significant changes in the beam power density in the irradiated area, resulting from defocusing, occur due to spot distortion, which is caused by changes in the beam’s position relative to the grinding wheel surface and the shape of that surface. Examples of spot shape changes are shown in Figure 3. As can be seen, the shape of the irradiation area created by a beam directed tangentially to the surface of the grinding wheel deviates from the original circular cross-section of the beam. The size of this area in the case of cylindrical grinding wheels can be determined using Equation 1[25] and 2 [23].

$$S_p = \frac{\pi d^2}{4cos(\theta + \alpha)} \tag{1}$$

where: *d* – laser beam diameter (mm), α – the central angle relative to the focal point on the surface of the circle, θ – the angle of incidence (0–90°) – Figure 4a.

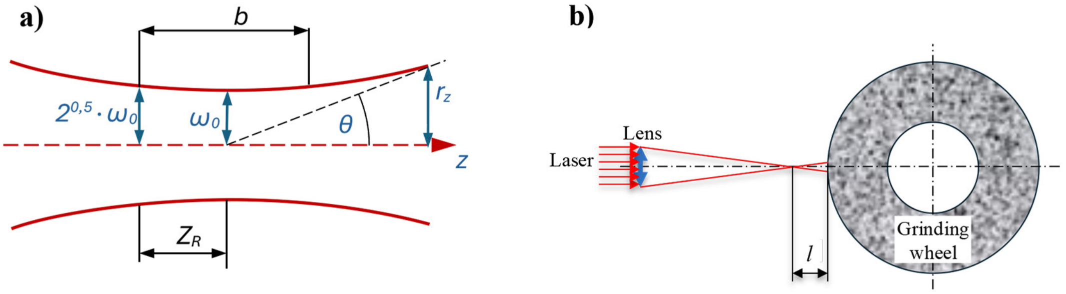

Figure 2. (a) Characteristics of laser beam, (b) position of the laser beam focal plane [22]

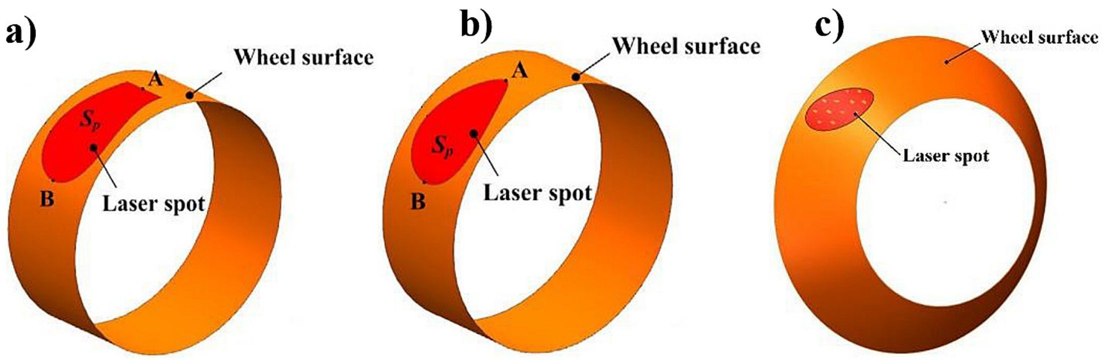

Figure 3. Geometry of the laser beam spot on the: (a, b) cylindrical [23], (c) conical [24] grinding wheel surface

$$S_p = \begin{cases} \displaystyle\int_{R-a}^{R} dx \int_{-\sqrt{r^2-(x-h)^2}}^{\sqrt{r^2-(x-h)^2}} \frac{R}{\sqrt{R^2-x^2}} dy, & 0 < a \le d \\ \displaystyle\int_{R-a}^{R-a+d} dx \int_{-\sqrt{r^2-(x-h)^2}}^{\sqrt{r^2-(x-h)^2}} \frac{R}{\sqrt{R^2-x^2}} dy, & d < a \le R \end{cases} \tag{2}$$

where: R – grinding wheel radius, a – dressing depth, d – focal spot diameter, r – focal spot radius, $h=R\text{-}a\text{+}d$.

When the grinding wheel is conical, Equation 3 [24] can be used to determine the size of the irradiation area.

$$S \approx S_0(1 + cot\alpha + cot^2\alpha) \tag{3}$$

where: S_0 – laser spot area on the cylindrical surface, α – inclination angle of the cone's generatrix relative to its base – Figure 4b.

For the ranges of the angle of incidence θ and the angle of the conical surface α (0–90°) (Figure 4a,b) the trigonometric functions used in Equations 1 and 3 take values ($0 < cos\theta < 1$, $cot\alpha > 0$), for which the surface area of the irradiation area increases with increasing angles. As a result, the power density of the laser radiation reaching the surface of the grinding wheel decreases. When using pulsed lasers, the approximate value of the radiation power density on the surface of the grinding wheel I_p can be calculated from Equation 4.

$$I_p = \frac{P_{avg}}{f\tau S_p} \tag{4}$$

where: P_{avg} – average laser radiation power, f – pulse repetition frequency, τ – pulse width (pulse duration), S_p – area of laser pulse impact on the grinding wheel surface.

The material from which the abrasive layer of the grinding wheel is made can only absorb part of this energy. This depends on its optical properties and the angle of incidence of the beam. The radiation absorption coefficient A_C can be determined using Equation 5, and the effective power

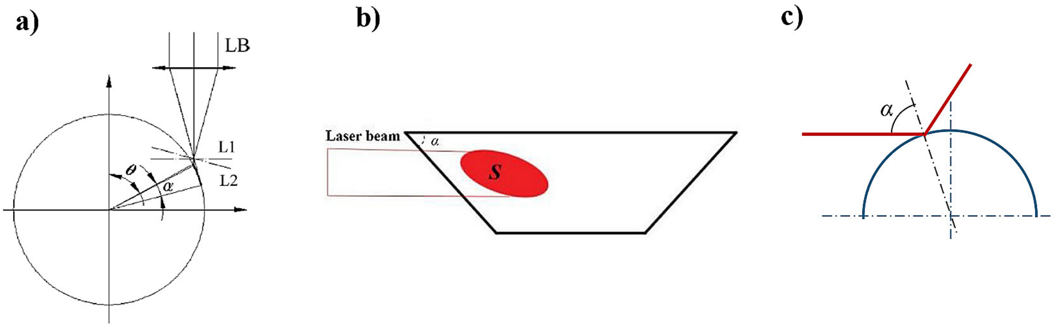

Figure 4. Auxiliary drawings (a) for Eq. (1) [25], (b) for Equation 3 [24], (c) for Equation 5

density absorbed by the abrasive layer I_A using Equation 6 [23].

$$A_C = 1 - \frac{(n\cos\alpha - 1)^2 + (k\cos\alpha)^2}{2(n\cos\alpha + 1)^2 + 2(k\cos\alpha)^2} - \frac{(n - \cos\alpha)^2 + k^2}{2(n + \cos\alpha)^2 + 2k^2} \tag{5}$$

where: α – incidence angle of the beam (Figure 4c), n – refractive index, k – extinction coefficient.

$$I_A = A_C \cdot I_p \tag{6}$$

The calculation results, changes in the amount of absorbed energy depending on the position of the laser beam (Figure 4a) relative to the cylindrical surface of the grinding wheel, are illustrated in the graph in Figure 5 [25]. The amount of energy that can be absorbed by the grinding wheel material decreases rapidly with increasing angle of incidence θ, e.g. for an angle of 60° it is 37.5% of the value determined for a beam incident perpendicularly (0°). When the cylindrical surface is irradiated with the laser at an increasingly larger angle θ approaching 90°, a moment occurs when the power density is so low that the ablation threshold is not exceeded and the grinding wheel material is not removed.

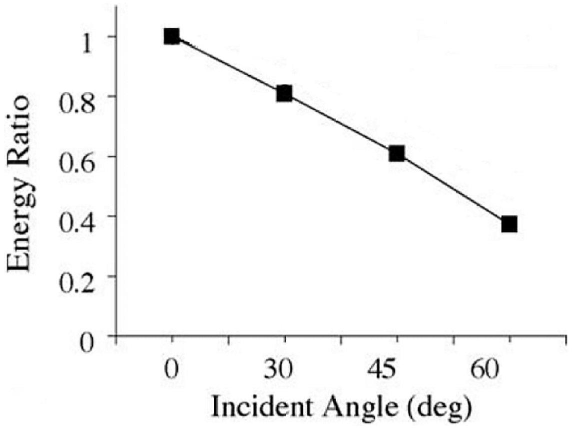

Figure 5. Effect of incident angle on absorbed energy [25]

Another cause of reduced power density at the irradiation point is the beam being blocked by the original surface, especially when the processing area is near the profile corner (section A-A in Figure 6). As a result, despite the focus being positioned on the grinding wheel surface, the power density at the irradiated point will decrease, affecting the ablation process. This occurs when dressing shaped surfaces with steep slopes, making it impossible to achieve the desired sidewall angle – especially a right angle.

Example graphs of the change in laser beam power density in the irradiated area, resulting from changes in spot size at various inclination angles α of the grinding wheel surface profile and dressing depth, are presented in Figure 7 [26]. As the grinding wheel profile becomes increasingly steep – angle α decreases – the power density gradually decreases, which affects the grinding wheel's material removal efficiency. When the power density does not exceed the material removal threshold, machining a profile with such an angle, at the applied machining depth, becomes impossible. Additionally, when the laser divergence angle θ (Figure 2a) is greater than the angle of the dressing profile α, the beam is obscured, further reducing its power on the grinding wheel surface and the ability to perform this angle.

In some cases, irradiating the grinding wheel surface with a defocused beam may be intentional, aimed at achieving the desired radiation density on the grinding wheel. As the distance between the focal plane and the grinding wheel surface, l (Figure 2b), increases, the laser spot size increases, which reduces the beam's power density on the grinding wheel surface. If the power density of the defocused beam is sufficient to remove grinding wheel material, the position of the focal plane will

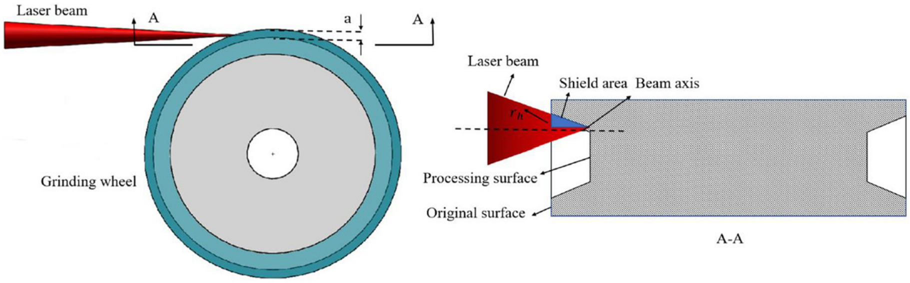

Figure 6. Material removal process of laser tangential dressing [24]

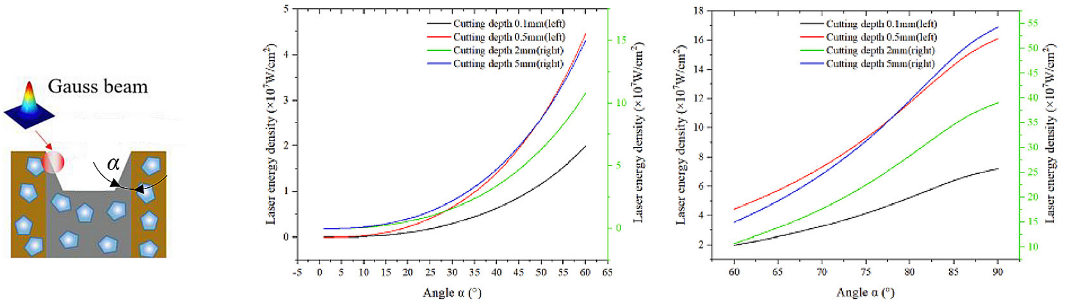

Figure 7. Laser energy density (I_α) vs dressing angle (α) [26]

determine the size of the ablated surface. An example of the effect of shifting the focal plane relative to the diamond grain surface on the width of the grooves created is shown in Figure 8 [27]. Regardless of the direction of focal plane shift (outward or into the diamond), the width of the microgrooves created by ablation increases. This phenomenon is slightly more intense when the focal plane is located above (the plus sign of the focal plane shift) rather than below the diamond surface.

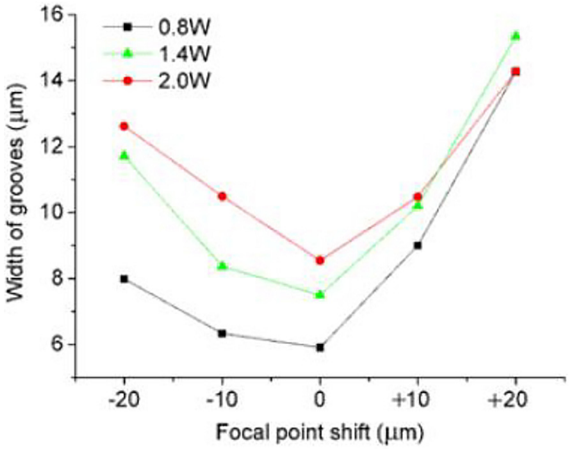

Figure 8. Influence of focal shift on width of groves. (PM laser: λ = 355 nm, τ = 132 ns, f = 25 kHz, d = 20 µm) [27]

It should also be noted that the power density of the laser beam is not uniform across the cross-section – the value decreases with distance from the beam axis. It is assumed to have a Gaussian distribution – Figure 9 [28].

The radiation power density I at any point defined by the defocus distance z and the distance r from the beam axis (Figure 2a) is calculated from the Equations 7, 8 [29,30].

$$I(r,z) = \frac{2W}{\pi r_z^2} \exp\left(-\frac{2r^2}{r_z^2}\right) \tag{7}$$

$$r_z = \left[\omega_0^2 + \left(\frac{z\lambda_0}{\pi\omega_0}\right)^2\right]^{0.5} \tag{8}$$

where: W – radiation power, ω_0 – beam radius in the focal plane, r_z – defocused beam radius at a distance z from the focal plane, λ_0 – laser wavelength.

Equation 7 and 8 indicate that the beam's power density decreases with increasing distance from the focus and from the beam axis. The laser

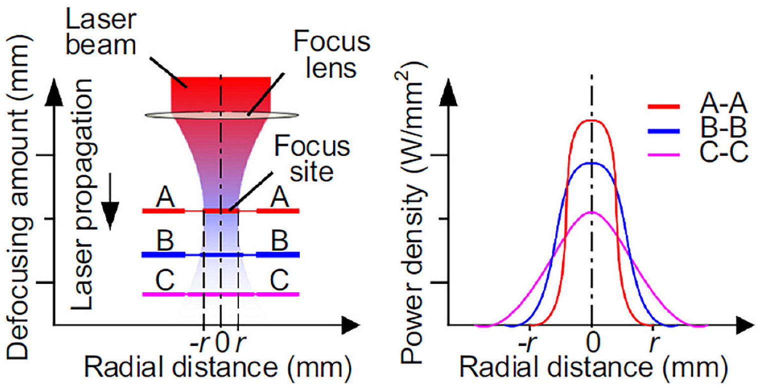

Figure 9. Power density distribution across the beam cross-section [28]

beam's ability to remove grinding wheel material changes in the same way. Therefore, in laser machining, it is impossible to unambiguously determine the position of the "tool tip," which has exactly the same effect on the grinding wheel material. However, it is assumed that the beam has similar properties within the so-called depth of focus. The depth of focus extends over a section equal to twice the Rayleigh length (z_R – Figure 2a), between two planes located on either side of the beam's focal spot, in which the beam radius is $2^{0.5}\cdot\omega_0$. The length of this section is calculated according to Equation 9.

$$b = 2z_R = \frac{2\pi\omega_0^2}{\lambda_0} \tag{9}$$

where: z_R – Rayleigh length, ω_0 – beam radius in the focal plane, λ_0 – laser wavelength.

Ablation process

As already mentioned, there are many types of lasers available on the market, the main characteristics of which are: operating mode (CWM – continuous wave mode; PM – pulsed mode) – Figure 10 – radiation wavelength λ and laser power P. In the case of lasers operating in pulsed mode, additional characteristics are: pulse frequency f and pulse width τ. In continuous beam mode, laser energy is discharged continuously for a long time. In pulsed mode, energy is stored until a threshold is reached. After reaching the threshold, the stored energy is quickly discharged in a short-duration pulse. A typical pulse shape is shown in Figure 10b. Each pulse is characterized by an initial power spike, the peak value of which is approximately two to three times higher than the average power during the pulse. After this initial spike, the power decreases [31].

An important feature of pulsed lasers is the pulse duration τ. The shorter the pulse, the faster the stored energy is released, allowing extremely high instantaneous radiation power to be achieved. For example, a femtosecond laser, which generates light pulses with an energy of 6 mJ and a duration of 30 fs (x10^{-15} s), has a peak power of approximately 200 GW (this is significantly higher than the power generated simultaneously, but continuously, by all power plants in Poland, which is approximately 62 GW).

Laser ablation of material is possible after exceeding the so-called ablation threshold, i.e. transferring the minimum energy necessary to initiate it. The ablation threshold value is a characteristic quantity for each material. The ablation process is described by two theories: thermodynamic transformations and Coulomb explosion. Both assume that energy absorption is the result of the interaction of the electric field of the beam with the electrons of the atoms of the irradiated material. However, the effect of this interaction depends on the time required to transfer the necessary amount of energy. If the energy is supplied continuously (CWM) or the pulse duration (PM) there are several orders of magnitude longer than the time required for energy exchange between electrons and the crystal lattice, the theory of thermodynamic transitions applies. Ablation is then the result of intense heat interaction [32]. It is assumed that the excited electrons transfer energy to the atomic lattice as a result of collisions with phonons, increasing the amplitude of the lattice wave and the quantised energy level. The temperature of the material increases, and it melts in the area of beam interaction. Part of the molten material begins to evaporate and ionise. The vapour causes a high increase in pressure in the volume of the molten material, causing it to be ejected and an ablation crater to form. The molten material that remains on the crater wall solidifies after the laser beam interaction ends, forming a layer on its surface [33].

The Coulomb explosion theory describes the ablation process in the case of transferring the required amount of energy in ultrashort pulses (pico- and femtosecond lasers). In this case, the time of energy exchange between electrons and ions and the time of heat conduction

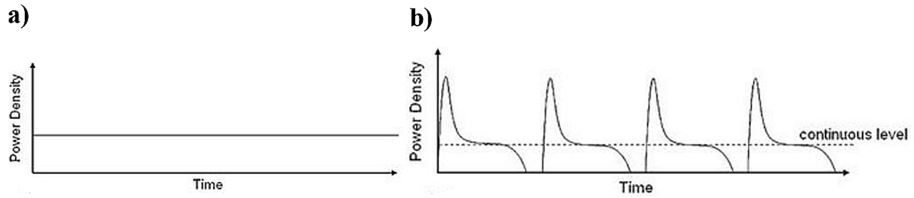

Figure 10. Temporal modes or laser operation: (a) continuous wave mode; (b) pulsed mode [31]

are significantly longer than the pulse duration. The energy delivered is therefore absorbed only by electrons, which, after exceeding the Fermi energy, escape from the system, leaving positively charged ions. This weakens the lattice bonds and, as a result of Coulomb repulsion, a plasma explosion occurs – the ejection of ions and electrons from the material. In this case, no energy is transferred to the lattice. The absorbed energy is dissipated by the removed material, so that no heat-affected zone is created in the material and the crystal lattice remains cool.

Figure 11 shows a schematic comparison, and Figure 12 shows microscopic images of the effects of laser ablation using long and ultrashort pulses. Surface damage and the formation of surface contaminants are typical for pulses in the ns–µs range. For ultrashort pulses, the heat-affected zone is negligible, and the defects mentioned earlier do not occur. The images in Figure 12a,b (ns and ps pulses) indicate the presence of molten material around the crater and hoops formed as a result of recoil vapor pressure. For femtosecond pulses (Figure 12c), only a ring of gaseous dust was formed around the crater. The photographs presented confirm the validity of the theory indicating that as the pulse duration decreases, the influence of thermodynamic changes on the course and outcome of ablation becomes increasingly smaller. Ultrafast laser ablation, due to its short pulse duration, generates a minimal heat-affected zone (HAZ) in the material, ensuring that the surface layer of the material does not change its properties after ablation.

Impact of the laser beam on diamond abrasive – graphitization

A negative consequence of the thermodynamic phenomena occurring on the diamond surface due to laser radiation absorption is its allotropic transformation into a less hard form – graphite. In an air atmosphere at a temperature of 750 °C, the diamond abrasive reacts with oxygen and softens. At temperatures around 1500 °C, the diamond transforms into graphite, causing a rapid decrease in its strength and hardness. This is very unfavorable for the cutting properties of diamond grinding wheels.

The degree of graphitization of diamond abrasives is assessed using Raman spectroscopy. The spectral peak at 1348.91 cm^{-1} is characteristic for diamond, while the peak at 1596.36 cm^{-1} is characteristic for graphite. The diamond abrasive particles in the grinding wheel contain

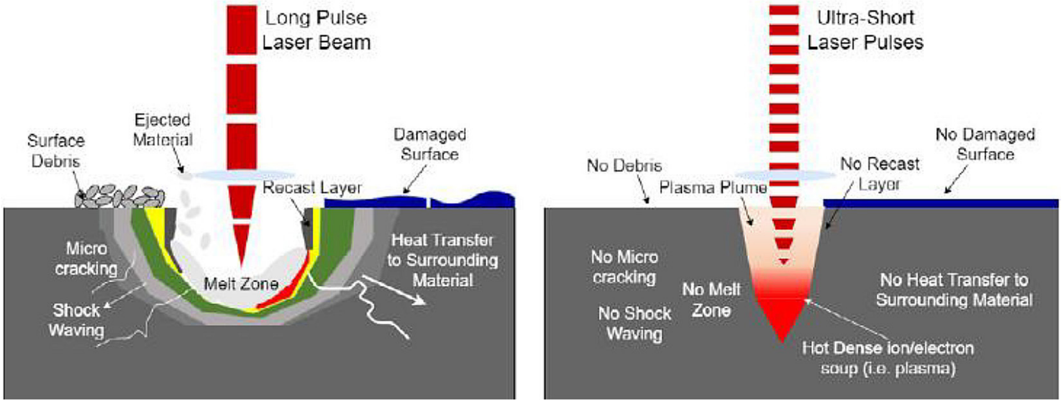

Figure 11. Description of phenomena in which the material undergoes when speaking of long and ultra-short laser pulses [34]

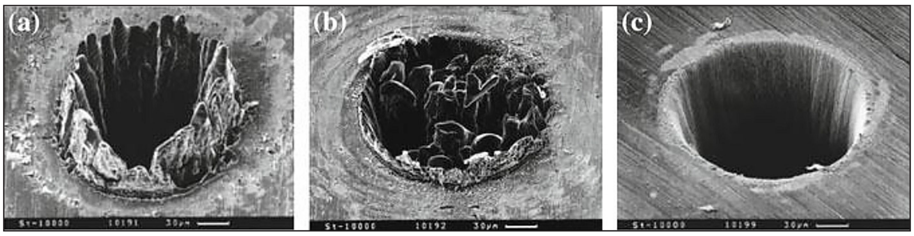

Figure 12. Craters with 100 microns diameter drilled in steel in vacuum (10^{-4} mbar), Laser Ti-safir with: (a) 3.3 ns (4.2 J/cm^2), (b) 80 ps (3.7 J/cm^2), (c) 200 fs (0.5 J/cm^2) [35]

certain impurities that can cause slight deviations in the characteristic Raman peak position. The degree of graphitization of the abrasive is defined by the β index, which is the ratio of the Raman peak intensity of the graphite IG spectral line to the intensity of the diamond ID spectral line [36]. The higher the β value, the greater the degree of graphitization. Figure 13 shows sample graphs of the Raman spectra of the diamond abrasive obtained from analysis performed after laser and electro-discharge dressing.

Kinematics parameters of the laser beam dressing process

In addition to the previously discussed parameters concerning the laser positioning relative to the grinding wheel and the beam characteristics, the result of conditioning the active grinding wheel surface is also influenced by kinematic parameters: grinding wheel rotational speed *n* and scanning feed rate *v*. If the laser operates in continuous mode (CWM), the resultant of combining both movements is a spiral formed on the grinding wheel surface, the coils of which have a width corresponding to the laser spot diameter. When operating in pulsed mode (PM), a spiral of spots is formed (Figure 14). Changes in rotational speed and scanning feed rate cause changes in the spiral pitch *L* and the mutual spot spacing *M*. Distance *M* results from the frequency *f* of the laser-generated pulses and the grinding wheel rotational speed *n*, and distance *L* from the scanning feed rate *v* and rotational speed *n*. Distances *M* and *L* can be determined from Equation 10 and Equation 11 [37].

$$M = \frac{\pi D n}{f} \tag{10}$$

$$L = \frac{v}{n} \tag{11}$$

where: D – grinding wheel diameter, n – grinding wheel rotational speed, v – scanning feed rate.

The U_D ratio, which determines the degree of overlap of the laser scanning path along the grinding wheel generatrix, is calculated according to Equation 12, and the U_P ratio of laser spot overlap according to Equation 13 [37].

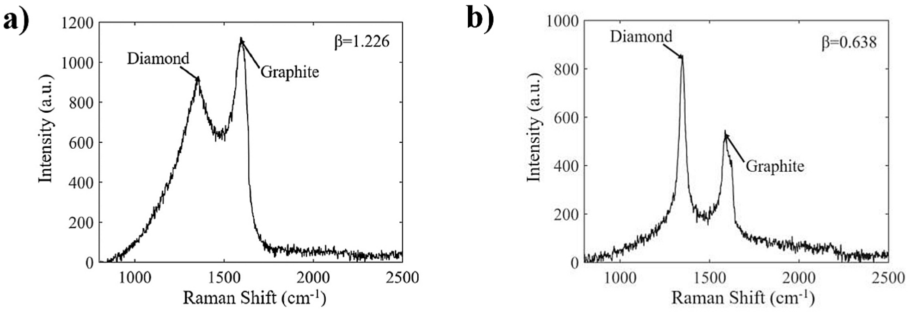

Figure 13. Raman spectra of the diamond abrasive particles after laser (a) and electrical discharge dressing (b) [36]

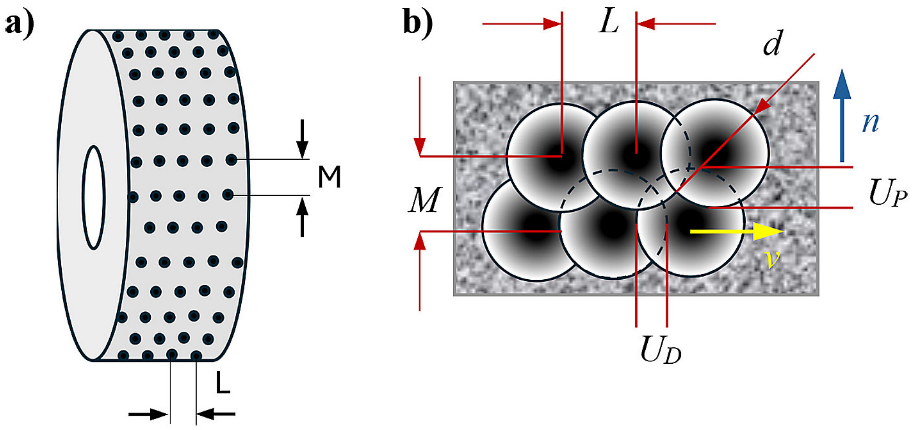

Figure 14. (a) Characterisation quantities of the laser beam trace on the grinding wheel surface *M*, *L*; (b) schematic diagram of laser pulse overlap rate U_P and line overlap rate of laser ablation tracks U_D

$$U_D = \frac{d - L}{d} \cdot 100\% \tag{12}$$

$$U_P = \frac{d - M}{d} \cdot 100\% \tag{13}$$

where: L – spiral pitch, M – spot spacing, d – laser spot diameter.

Higher values of the ratios indicate a tighter packing of the craters formed. A graphical interpretation of the ratios is presented in the diagram in Figure 14b.

An example of the influence of the adjustable parameters of the laser beam dressing process is provided by the results of research which assessed the effect of scanning feed rate and grinding wheel rotational speed on the obtained surface roughness of a bronze bond. By varying the parameters within the range of 10–70% at the same laser beam power, the distribution of ablation craters was analyzed, and the surface roughness was measured. It was found that with increasing values of the ratios, the density of laser ablation craters increased, and the bond surface smoothness improved and was the highest when $U_D = U_P = 70\%$.

LASER METHODS FOR DRESSING OF SUPERABRASIVE PROFILE GRINDING WHEELS

Laser machining of shaped grooves with a tangential beam

A pulsed Q-switched fiber laser (λ = 1064 nm, P_{avg} = 30-48 W, τ < 200 ns, f = 50 kHz) was used to shape profiles, which are visible in Figure 15 [39], on mounted CBN grinding wheels with a hybrid (ceramic-metal) bond. Dressing was performed on a 5-axis milling machine equipped with a high-speed grinding spindle (f_s = 2000 Hz). Profiling was performed through a tangential incident laser beam, with a radial infeed of a_r = 0.1 mm. Compressed air at a pressure of p_{air} = 5 bar was used to remove ablation products and cool the grinding wheel surface. Preliminary tests to investigate the ablation behavior of the abrasive and binder have shown that effective laser ablation of CBN grains occurs when the laser pulse energy is greater than 0.5 mJ (corresponding to P_{avg} = 25 W at f = 50 kHz). Using higher laser beam powers, a combination of the remaining dressing parameters (U_D, U_P) was investigated,

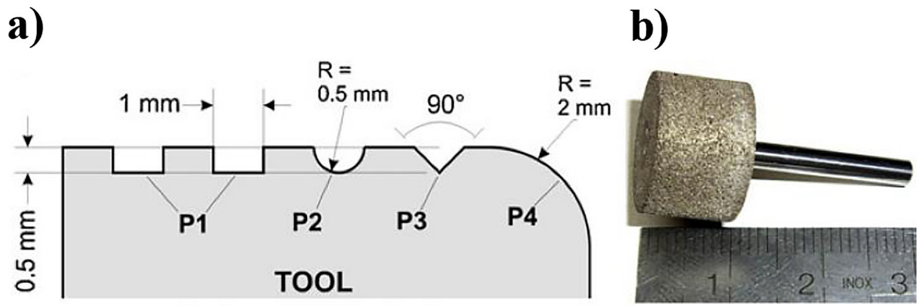

Figure 15. (a) Dimensions of the trued profiles P1–P4, (b) hybrid bonded mounted wheel [39]

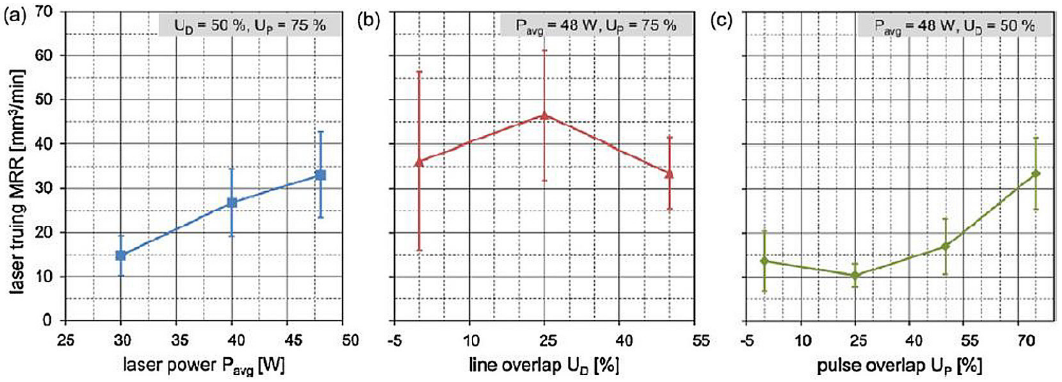

Figure 16. (a) Influence of laser power, (b) line overlap, c) pulse overlap on the material removal rate (MRR) of the laser truing process [39]

that would provide the highest ablation efficiency. The graphs of the test results are shown in Figure 16. Laser power has a clear, proportional effect on the material removal rate (Figure 16a). Laser beam feed, which determines path overlap (U_D), and tool rotational speed, which determines spot overlap (U_P), also exhibit a significant but variable effect on ablation rate. Initially reducing the feed rate (Figure 16b) resulted in an increase in efficiency but then caused a decrease. Reducing the grinding wheel speed (Figure 16c) initially caused a decrease, and then an increase in ablation efficiency.

The dressing results were considered satisfactory, particularly in shaping the sharp end of the bottom of the P3 profile (Figure 17a). The tip rounding radius on a workpiece made of hardened 100Cr6 bearing steel (60 ±1 HRC), ground with a grinding wheel thus dressed, did not exceed 20 µm (Figure 17b). This result was attributed to the use of a fiber laser, whose focused beam was characterized by a very small spot size and low divergence, as well as the dressing parameters adopted, which ensured, in addition to binder ablation, precise machining of the abrasive grains. The achieved grinding accuracy was comparable to the grain size used in the grinding wheel (B126). Shaping the P1 profile was less accurate. Here, the side edges of the profile are not perpendicular to its bottom. It should be assumed that this is a consequence of the reduction in the beam power density due to its defocusing and blocking by the original surface (Figure 6, Figure 7).

The negative result of the dressing was a smooth grinding wheel surface (Figure 18b). No spaces for chips were created, resulting in higher grinding forces in the initial period of the grinding wheel's operation (Figure 18a). The subsequent reduction in these forces was related to the self-sharpening of the grinding wheel through the loss of binder around the grains, as confirmed by SEM images (Figure 18c). The authors of the method concluded that, due to the preservation of the profile edge quality, self-sharpening the grinding wheel during grinding is a better choice than sharpening it after laser processing using a corundum block.

Laser machining with a deflected tangential beam

In [24,26,29,38] the conditions related to the use of a tangentially directed beam to form grooves in the abrasive layer were considered:

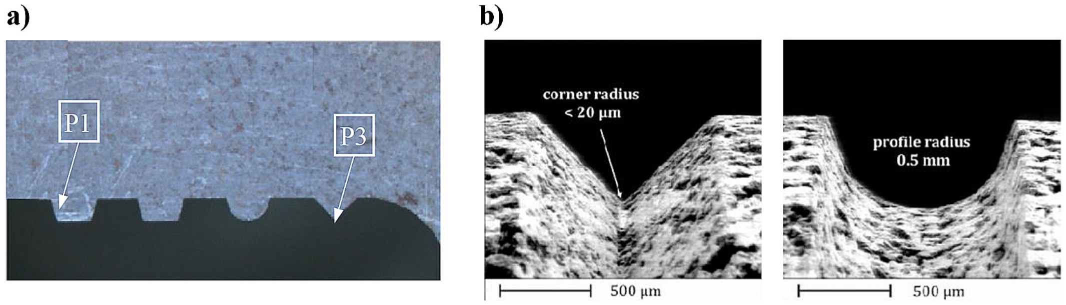

Figure 17. (a) ground workpiece profile, (b) microphotograph of the P2 and P3 profiles on a dressed grinding wheel [39

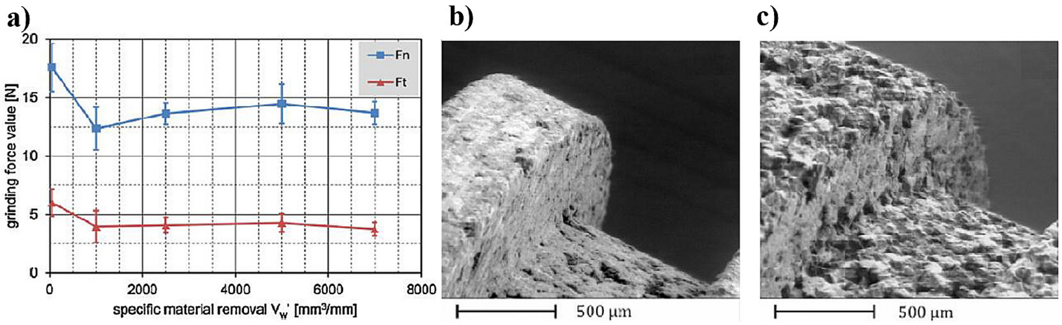

Figure 18. (a) Grinding forces, SEM micrograph: (b) newly trued grinding wheel, (c) after 7000 mm^3/mm specific material removal [39]

with perpendicular walls [29], with walls inclined at specific angles with arc-shaped transitions (Figure 19a,b) [24,26], as well as to form a bevel at a specific angle on the grinding wheel edge [38] – Figure 19c. The research concerned the formation of the above-mentioned profiles in bronze-bonded diamond grinding wheels using a nanosecond fiber laser (λ = 1064 nm, P_{avg} = 100 W, τ = 60–100 ns, f = 100 kHz, d = 38 µm). To avoid errors resulting from beam defocusing (Figure 3) and its obscuration by the primary profile (Figure 6), the standard method of laser positioning was modified by deflecting it at a small angle Θ, as shown in Figure 20 and Figure 21. The effect of this procedure is to reduce the size of the resulting dressing error (side wall inclination deviation), and by reducing the size of the laser spot on the side walls of the profiles, to increase the radiation power density in the ablation area and its intensification.

The change in the process accuracy of the groove side walls resulting from the laser beam deflection is presented in the graphs in Figure 22. The desired groove wall inclination angle was obtained when the laser deflection angle Θ exceeded 1° and 1.5° (Figure 22a). A larger laser deflection was required for machining the wall inclined at a smaller angle (7.78°). Exceeding the indicated deviations resulted in a deterioration of the PV accuracy of the processed profile (Figure 22b). The

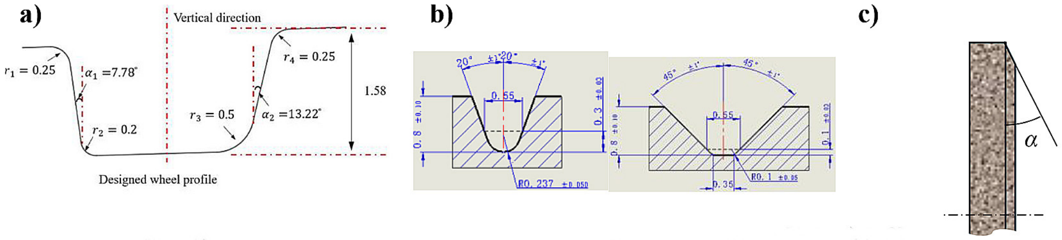

Figure 19. Profiles shaped by laser tangential beam: (a) [24], (b) [26], (c) [38]

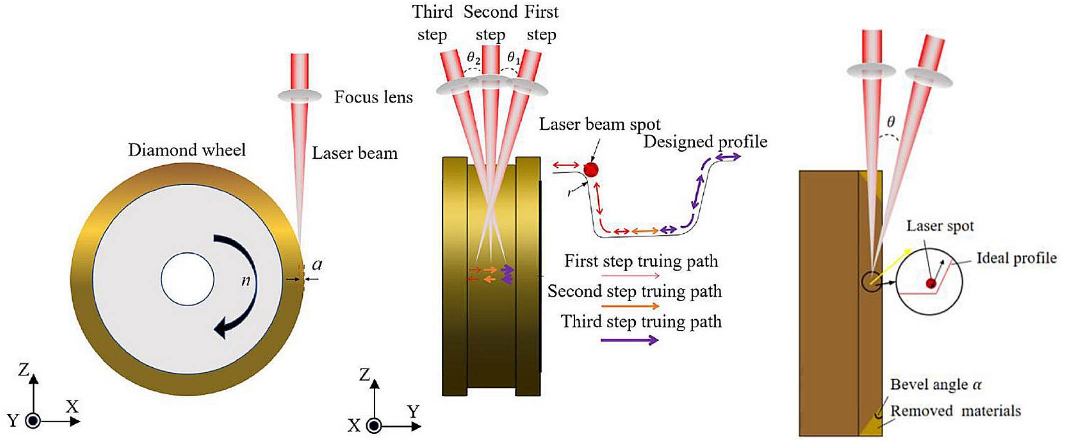

Figure 20. Tangential profiling of a deflected laser beam bronze bonded diamond grinding wheel [24,38]

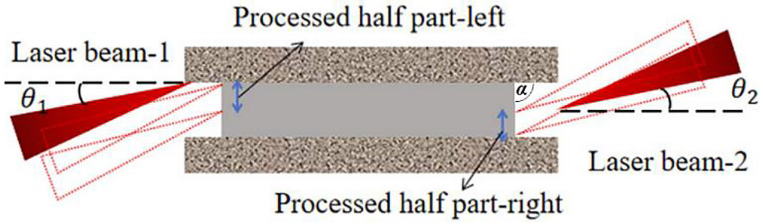

Figure 21. Schematic diagram of the laser dressing concave rectangular grinding wheels process: laser dressing process by deflectable dual-laser misaligned tangential [29]

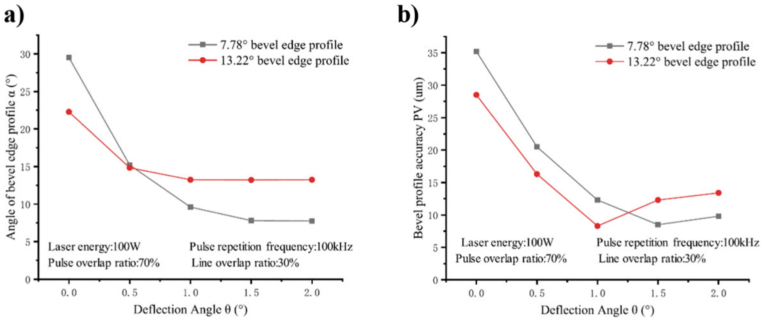

Figure 22. (a, b) Angle *α* and PV accuracy of bevel edge profile vs. deflection angle *Θ* [24]

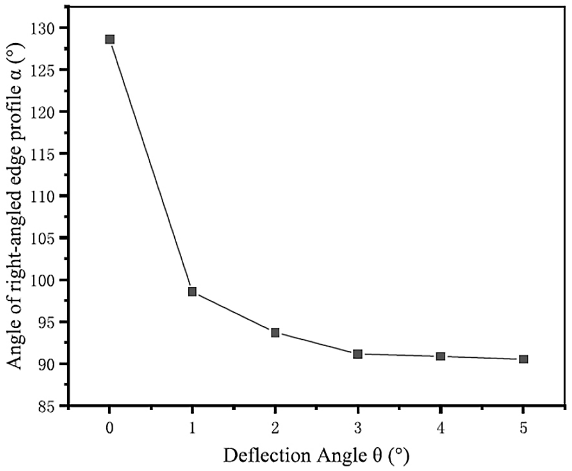

Figure 23. Contour accuracy diagram: laser deflection angle Θ vs. angle of right-angled contour *α* [29]

authors of the study associate this effect with the increase in energy concentration in the laser beam spot (compare the graph in Figure 7). This results in an increased diamond and binder material removal rate, which is associated with lower ablation accuracy. In the case of shaping walls perpendicular to the groove bottom, the laser beam direction required a larger deviation (Figure 23) [29]. The smallest error (0.51°) was achieved when ablation was performed with the beam deflected by 5°.

While shaping a groove with arc-shaped transitions using a laser beam directed tangentially to the grinding wheel surface, the authors [24] noted that guiding the beam along a path consistent with the designed profile resulted in errors in the radii of the formed fillets. Concave arcs had radii smaller than the designed ones, while convex arcs had larger radii. To achieve the required arc curvature, the beam guidance path must be corrected – for concave arcs, the path radius must be increased (Figure 24a) and for convex arcs, it must be decreased (Figure 24b). The amount of radius compensation *Δr* for the given ablation conditions is selected experimentally (the method is described later in the paper).

By using laser beam deflection and arc radius compensation, high accuracy was achieved in ablation a groove with inclined walls and arc transitions [24]. The final PV (peak to valley) value of the inclined groove wall was approximately 8 μm, and the arc radius error was 10 μm. A similarly high accuracy was observed in ablation the profiles shown in Figure 19b [26]. Using laser spot and path overlap of U_P=30%, U_D=80%, respectively, the deviation of the trapezoidal profile angle did not exceed 0.281°, the change of the arc radius was 4.9%, the profile height was 3.74%, and in the case of the V-shaped profile, 0.293°, 1.22%, and 3.18%, respectively. However, the use of a nanosecond laser caused graphitization of the diamond abrasive. Raman spectroscopic measurements showed that the degree of graphitization determined by the graphitization index was approximately 0.3 [29,38].

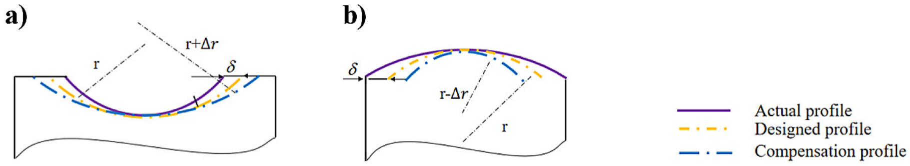

Figure 24. Radius error compensation of convex and concave surface grinding wheel (a) concave arc profile; (b) convex arc profile [24]

Laser machining of deep grinding wheel profiles

During scanning a deep grinding wheel contour with a tangential beam, significant changes in the power density of the radiation reaching the grinding wheel surface occur. This is the result of changes in the distance of the designed ablation point from the beam focal plane (Δ_i) and changes in the beam incidence angle (α_i) – Figure 25a. When profiling grinding wheels with a deep contour, the reduction in power density may be so great that the beam loses its ability to remove material along a certain section of its path, which significantly reduces the efficiency of the profiling process.

A description of the method for efficiently shaping a deep grinding wheel contour with a tangential beam can be found in [45],[40] and [42].

In [45] the problem was considered using the example of shaping a V-shaped profile on a cylindrical grinding wheel. A method for designing a beam trajectory that minimizes the time required for the operation was proposed. The essence of the proposed solution is to periodically shift the focal plane to bring subsequent areas of the grinding wheel surface into the zone of the beam's ablation capability. Initially, the focal plane is positioned at the intersection of the grinding wheel's lateral surface with the projection of the designed profile onto the cylindrical grinding wheel's surface (point A_0, Figure 25a). After scanning, but only over the section where the beam does not lose its ability to ablate the material (point B), the focal plane is shifted by the designed value (Δ_z, Figure 25b) towards the grinding wheel, and scanning continues along the section from the starting point (A_0) to the point where the beam demonstrates its ability to ablate the material. This cycle repeats until the focal plane is aligned with the cross-sectional plane through the grinding wheel diameter (point A) – Figure 34b. The number of focal plane shifts required depends on the number of times the beam loses its ablation ability, which is a function of the profile depth, grinding wheel diameter, laser power, and the grinding wheel material characterized by its ablation threshold.

The experimental research used a pulsed laser (P_{avg} 20–70 W, $\lambda = 1064$ nm, $d = 28$ µm, $\tau = 20$ ns, $f = 50$ kHz) and a resin-bonded diamond grinding wheel 85 mm in diameter and 9 mm wide (grain size approximately 120 µm). To determine the location of the points at which ablation ceases, it is necessary to know the threshold power density value for a given material. The diamond ablation threshold was determined in the described research using spectral monitoring. During profiling with a laser operating at various power levels (20, 50, 70 W), the spectra of the formed plasma were observed with a spectrometer. The appearance and intensity of a selected spectral line characteristic of diamond indicated that the diamond was undergoing ablation. Calculation of the radiation power density at the moment of ablation termination, based on theoretical Equation 4, 5, 6, determined the diamond ablation threshold. The test results indicated a value of 3.0×10^7 W/cm^2. Knowing this value, the same Equation can be used to calculate the length of the beam trajectory section where ablation occurs (AB, Figure 25a) and the required focal plane position. The authors, however, pointing to the simplification of trajectory design and the ablation process itself, propose

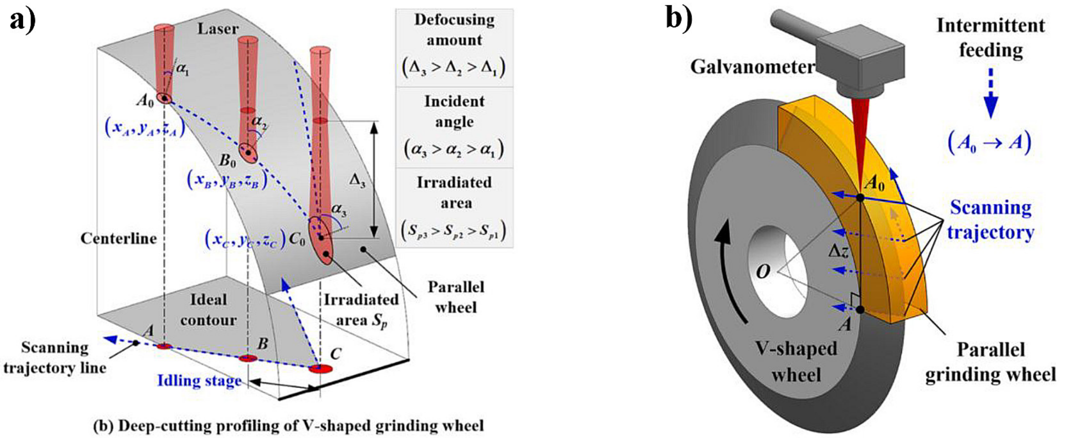

Figure 25. (a) Defocusing and beam incident angle variation during deep-cutting laser profiling, (b) laser beam intermittent feeding in deep-cutting laser profiling of V-shaped grinding wheel [45]

slightly extending the ablation section and, consequently, setting the beam focal plane displacement step to a value equal to five times the Rayleigh length. The calculated trajectory sections proved to be very close to the actual ones – Figure 26. During profiling, in which both the grinding wheel and the laser beam moved at a constant speed, the time the diamond-specific spectral line remained at a specific intensity level was measured. The length of the section where ablation occurred was calculated using the Equation in Figure 26b. The observed deviations between the theoretical and actual section lengths were explained by the spectrometer's inertia, which lengthens its response when the intensity of the analyzed radiation is higher. This occurs at the beginning of profiling, when the beam angle is the smallest, resulting in the highest power density on the grinding wheel surface and more intense ablation. The contour profiling time using the segmented scanning method was 0.85 hours shorter than the standard method, which took 4.13 hours – Figure 27a. Profile accuracy tests confirmed that the laser beam shaped the diamond grains. The V-profile peaks had smaller rounding radii than the diamond grains used to construct the grinding wheel – Figure 27b.

In [40] a method for shaping a surface with an arc profile was presented. A cylindrical diamond grinding wheel was trued. This method uses an adapted "single-layer deep-cutting intermittent feeding method" developed by the authors of [23, 41] – Figure 28b. The essence of the new method is the parallel shift of the tangential beam towards the grinding wheel axis and setting the beam focus at point A on the grinding wheel edge – Figure 28a. The amount of shift is determined by the allowance a_p, which is to ensure the leveling of the radial run-out of the grinding wheel surface, and the height x of the arc (a_p+x). From this point, the beam scans the grinding wheel surface at a constant speed v, performing reciprocating movements along the arc-shaped trajectory. During profiling, the grinding wheel rotates at a constant speed. After completing subsequent scanning cycles, determined based on acoustic and optical signals generated during the laser ablation process, the beam focus is gradually moved along the section d_z until point C is reached.

The accuracy of the beam positioning at point A determines whether the arc will be symmetrically positioned relative to the radial axis of symmetry of the grinding wheel. To ensure very accurate beam positioning, the authors of [40] developed a method using the acoustic emission signal generated during contact of laser radiation with the grinding wheel material – Figure 29.

By recording the times: scan start (at point c_0), contact with the grinding wheel (c_1), contact end (c_2), and scan end (c_3), for a known scanning speed v, it is possible to determine the actual position

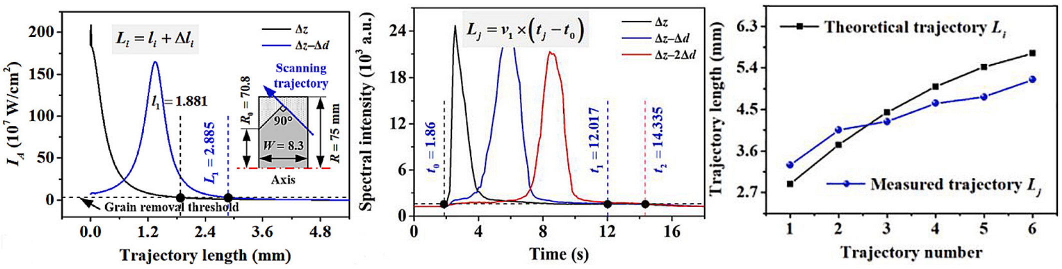

Figure 26. Theoretical and measured trajectory length [45]

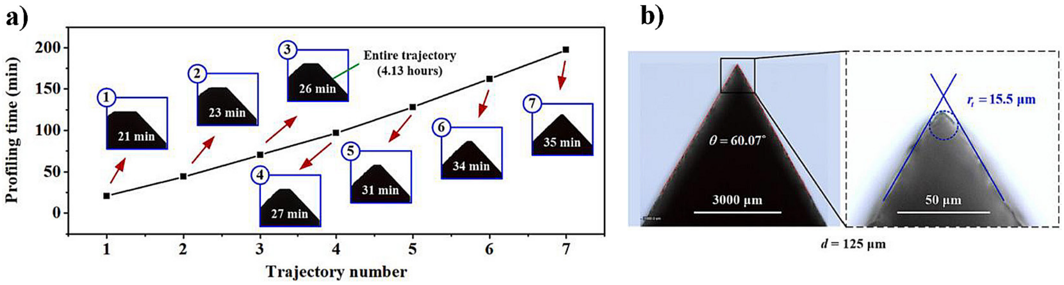

Figure 27. (a) profiling time: left outline - segment method, right outline - standard method, (b) axial sectional contour accuracy of grinding wheel after profiling [45]

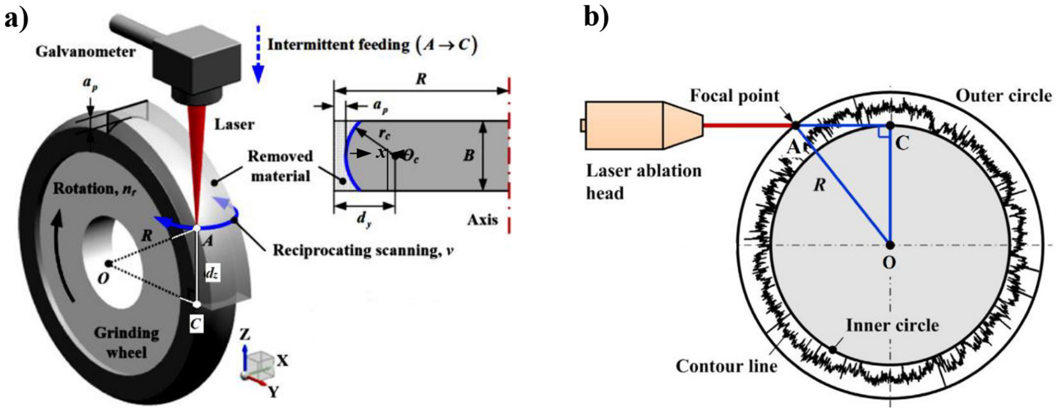

Figure 28. Schematic diagram of laser profiling [40,23]

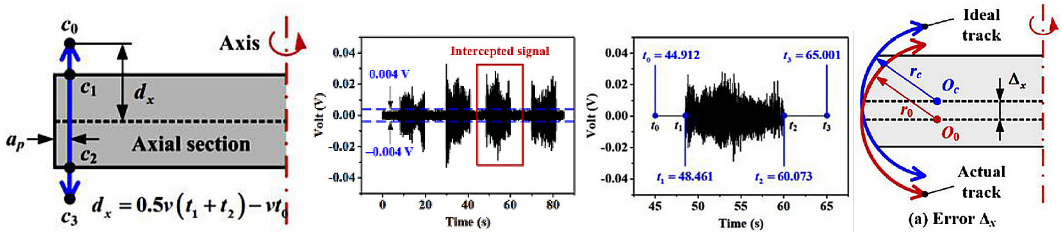

Figure 29. Schematic diagram of tool setting of laser beam [40]

of the grinding wheel symmetry axis (d_x) and the required correction (Δ_x) of the scanning arc center position. The authors estimate that by monitoring acoustic emission, laser beam alignment accuracy at the micron level can be achieved. The methods described above were used to profile an arc with a radius of r_c = 4.4 on a 150 mm diameter, 5.8 mm wide, and 180 µm grain size resin-bonded diamond grinding wheel. The grinding wheel was profiled using a pulsed laser (λ = 1064 nm, d = 28 µm, τ = 20 ns, f = 50 kHz). The pulse energy during profiling was 0.8 mJ. After profiling, the circular runout error of the crosssectional contour of the arc-shaped grinding wheel was about 22.1 µm, and the position error of the axial sectional contour was about 15.4 µm, the dimensional error was about 14.3 µm and the roundness error was about 17.4 µm.

A unique method for sharpening arc-shaped grinding wheel with a radial beam was also proposed. The essence of this method is to scan the grinding wheel surface with a beam whose focus moves along a path parallel to the grinding wheel axis (Figure 30). The first scan is performed with the focus positioned at the apex of the arc (point A_1), and subsequent scans are performed after moving the focus toward the axis by the Rayleigh length L_R. The total length of the focus moving must correspond to the arc height.

Tests conducted after profiling and sharpening showed that 90% of the diamond grains on the grinding wheel surface properly protruded above the bond (1/3 of the grain size). The graphitization of the grain surface, as recorded after profiling, did not increase as a result of sharpening. The lower laser pulse energy (0.1 mJ) was sufficient to ablate the resin bond but did not induce the diamond temperature increase necessary for the allotropic transformation to graphite. The degree of graphitization was not uniform across the grinding

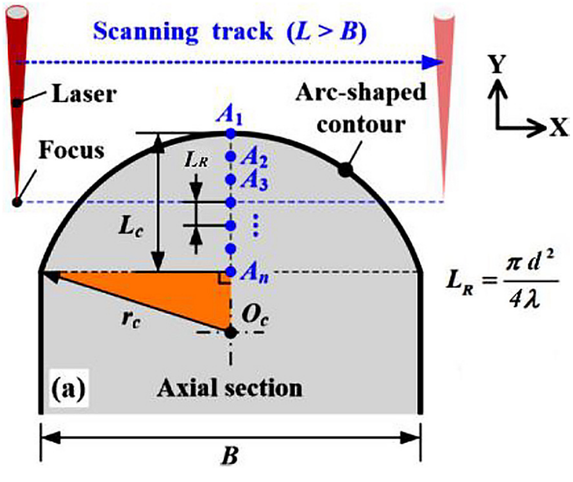

Figure 30. Schematic diagram of laser sharpening [40]

wheel surface. Raman spectra showed that grains located closer to the edge were more graphitized ($\beta \approx 1.07$) than those at the arc tip ($\beta \approx 0.23$).

Another method for machining a deep profile was presented in [42]. The technological process was divided into two stages. In the first stage, intended for rough shaping of the designed profile from a cylindrical blank, a radial laser beam was employed. In the second, finishing stage, a deflected tangential beam were used. The experimental investigations were carried out on a metal-bonded diamond grinding wheel. The blank is machined at a special ablation setup where the movement of the beam relative to the workpiece is achieved solely by mechanical axes, without the use of a laser scanning head – Figure 31f.

The control system maintains a constant peripheral speed v_s of the grinding wheel surface during machining. This ensures that changing the radius of the machined surface does not affect the U_P overlap ratio – the density of pulsed ablation craters remains constant along the entire circumference of the grinding wheel. The method involves three laser processing stages (Figure 31): radial roughing (a), quasi-tangential roughing and finishing (c), and final radial sharpening (e). Orthogonal machining is characterized by high ablation speed, but results in low dimensional accuracy, hence its positioning first in the process. Inaccuracy also results from changes in the radiation power density in the spot area on the oblique surfaces of the profile (Figure 4b, Figure 31d), where ablation is less intense. To leave the correct allowances for the next processing stage, the laser path is corrected relative to the designed profile. The axial shift x_c compensates for the lower ablation rate on the profile flanks, and the radial shift r_c compensates for radial ablation errors (Figure 31b). In the second stage, quasi-tangential roughing and finishing occurs (Figure 31c). The beam is here slightly deflected from the tangential direction toward the blank and removes a layer of thickness l_r in each pass. The lower ablation efficiency on the profile flanks is compensated for in this stage by reducing the feed rate. The final stage is sharpening (Figure 31e). The process is carried out with an order of magnitude lower beam power to remove only a small portion of the binder to expose the cutting grains on the surface.

Research into the material removal efficiency of various laser types led to the selection of a near-infrared (NIR) picosecond laser (λ = 1030 nm, d = 46 µm, τ = 10 ps, f = 800 kHz). A beneficial effect of using a picosecond laser was the absence of metamorphic transformations in the diamond. Raman spectra of diamond grains obtained after radial and tangential roughing did not reveal spectral line characteristic of graphite (Figure 32b). After sharpening, the surface appearance of the profile was comparable to that of the grinding wheel blank (Figure 32c).

Modification of the beam path in finishing

The inhomogeneity of the grinding wheel material and its structure results in variable ablation conditions. As a result of defocusing of the beam irradiating the grinding wheel surface, the ablation intensity becomes non-uniform, particularly in the regions of arcs and lateral profile surfaces. Achieving an accurate reproduction of the profile under such conditions requires multiple passes of the laser beam along the designed contour, without radial infeed into the wheel. However, this approach is time-consuming. To shorten

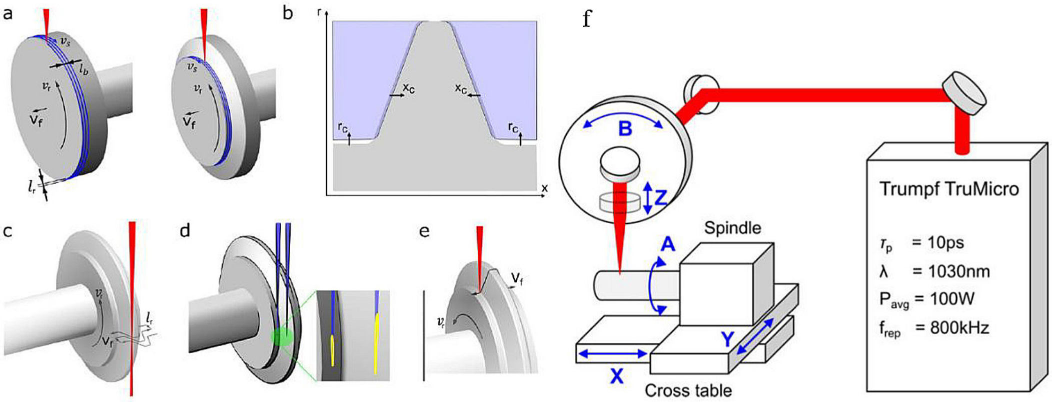

Figure 31. The laser manufacturing of high-precision grinding wheels [42]

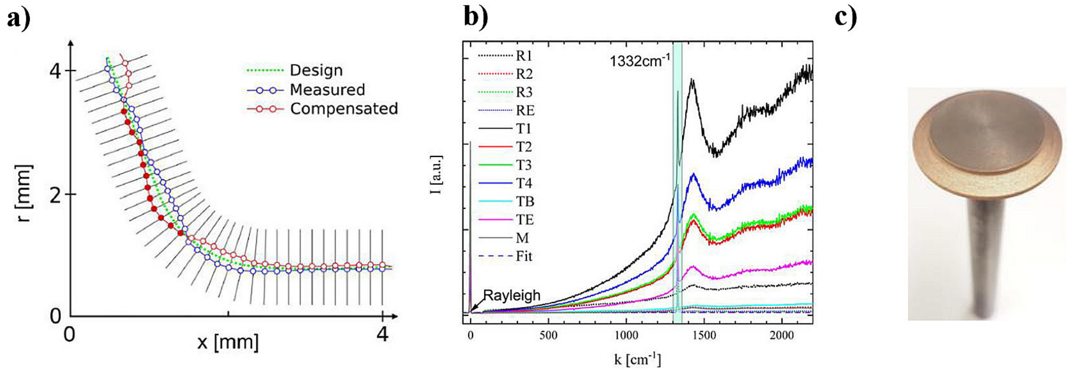

Figure 32. (a) Compensation strategy, (b) Raman spectra after laser machining, c) surface quality after the sharpening process [42]

this stage of the process, studies [42–44] proposed strategies for modifying the beam path based on profile errors determined from measurements.

In [42] the measurements of the grinding wheel profile after quasi-tangential finishing were performed on a Zoller Venturion 450 measuring machine. In places where excess material was found, the laser beam path is shifted deeper into the designed profile by the deviation value (Figure 32a), and in areas within tolerance, the beam feed rate is increased. The final accuracy of the profile formed using the described method was within ±3 μm.

A similar approach to obtaining the exact shape of the grinding wheel profile is presented in [43] and [44]. In both cases, after rough machining, finishing machining is performed, in which the laser moves relative to the grinding wheel along a specially designed path to compensate for rough machining errors. The profiling of the grinding wheel is performed here on a numerically controlled grinder with a laser beam tangentially incident on the wheel surface. Unlike [42], the grinding wheel is not dismantled to be measured on a separate device, but its profile is assessed based on the contour of a graphite plate ground with a pre-dressed grinding wheel on a measuring device installed directly on the grinder (Figure 33). Machining errors are assessed by comparing the actual profile with the designed profile. To achieve a high-precision profile, a tool path is designed to compensate for the resulting errors.

A nanosecond fiber optic laser (P_{avg} up to 100 W, λ = 1064 nm, d = 38 μm, τ = 100 ns, f = 5-100 kHz) was used to remove the abrasive layer. The measuring devices mounted on the grinder were enclosed in dust- and waterproof housing to protect against aerosol generated during dressing and grinding. Forced air circulation within the housing and a brush additionally prevented dust and aerosol from entering the measurement zone. The measurement involved computer analysis of the image obtained during CCD camera observation of a graphite plate, which was illuminated from below with parallel light. The CCD camera

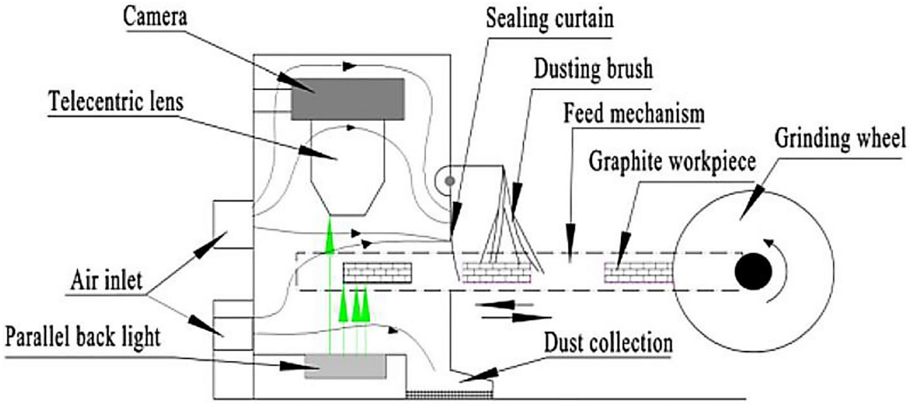

Figure 33. Experimental setup [43]

matrix had a resolution of 29 million pixels. The pixel size (approximately 3 µm) was the system's resolution limit. The adopted methodology was tested by machining a V-shaped groove on a bronze-bonded diamond grinding wheel [43] with grain size of approximately 120 µm, diameter 120 mm, and width 12 mm. The laser profiling parameter values were: P_{avg} = 100 W, f = 50 kHz, U_P = 70%, U_D = 30%. Measurements of a graphite plate ground with a roughly dressed grinding wheel showed that there were discrepancies with the designed profile, and the deviations were not uniform along the entire length of the profile and varied irregularly – Figure 34.

The smallest distance between the laser path in roughing and the resulting profile was defined as the effective dressing radius. The path along which the laser beam should travel in finishing was determined by shifting each point of the designed contour by the effective dressing radius – Equation 14, 15.

$$D_i = |P_i - R_i| = [|u_i - m_i|, |v_i - n_i|] \quad (14)$$

$$Q_i[s_{i,}t_i] \approx S_i \pm D_i = [x_i \pm |u_i - m_i|, y_i \pm |v_i - n_i|] \quad (15)$$

where: D_i – distance of the profile after rough machining from the rough machining path, $P_i[u_i, v_i]$, – set of rough contour points, $R_i[m_i, n_i]$ – set of rough machining path points, $S_i[x_i, y_i]$ – set of design contour points, $Q_i[s_i, t_i]$ – set of finishing machining path points.

In Equation 15, the „+" sign is used to compensate for the tool path on the left side of the profile, and the „–" sign is used on the right side of the profile. As a result of the applied compensation, the entire groove geometry was improved: its width, the shape of the walls, and the fillet radius of the groove bottom. The changes in the groove geometry dimensions after both types of machining are presented in Table 1 and Figure 35.

Using the experimental setup schematically shown in Figure 33, the possibility of precisely profiling a concave arc on the surface of a bronze-bonded diamond grinding wheel was also investigated – Figure 36a [44]. A 100 mm diameter, 8 mm wide grinding wheel with 230# diamonds was used for the tests. The grinding wheel was profiled with a laser beam with a power of P_{avg} = 80 W and a pulse repetition frequency of f = 100 kHz. The grinding wheel rotational speed and feed rate were set to achieve coverage indices of U_P = 70% and U_D = 30%. A computer image analysis program, whose algorithm enabled sub-pixel localization, was used to measure the contours of the graphite plate. The accuracy of edge detection in the processed image increased to 2.4 µm. The groove arc was shaped in several passes by removing successive layers of a_{pi} thickness. Before the first pass, the laser was positioned so that the beam focus was at the highest point of the grinding wheel. Arc measurements taken after each pass showed an increase in the shape deviation, with the highest values recorded on the outer sides of the arc. To compensate for this profile inaccuracy, the authors proposed an iterative horizontal compensation method. The minimum value of the horizontal component of the deviation, δ_{ih}, was determined (Figure 36b), which, depending on the side of the arc being corrected,

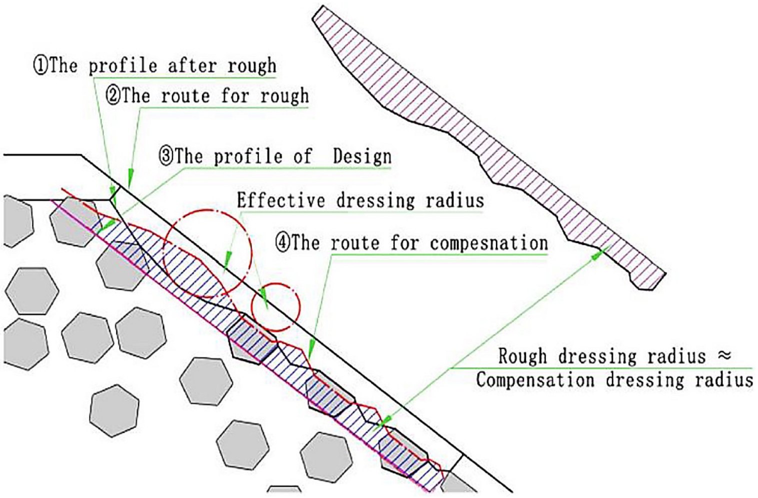

Figure 34. Principle of compensation algorithm [43]

Table 1. Geometry size after profiling [43]

Profiling	Depth [mm]	Width [mm]	Left angle [°]	Right angle [°]	Angle [°]	Difference [°]	Radius [µm]
Design	0.5	1	45	45	90	0	0
Rough	0.474	0.954	42.0	46.4	88.4	−2.4	45.3
Compensation	0.495	0.993	44.6	44.3	88.9	0.3	32.4

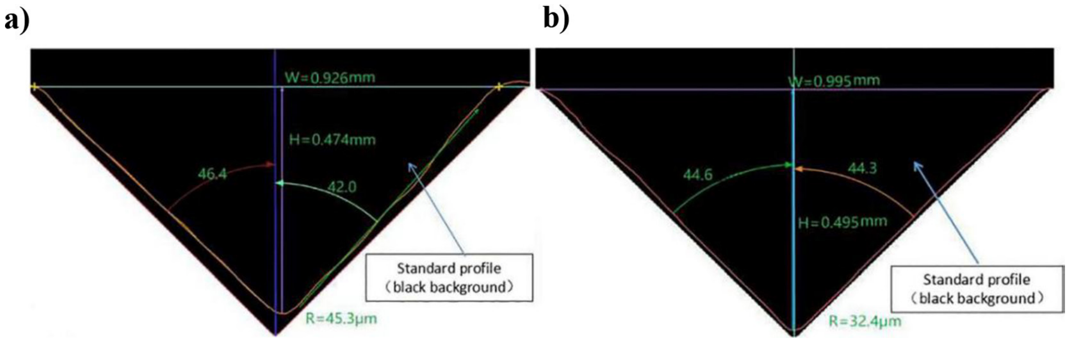

Figure 35. V-shape geometry after: (a) rough profiling, (b) finish profiling [43]

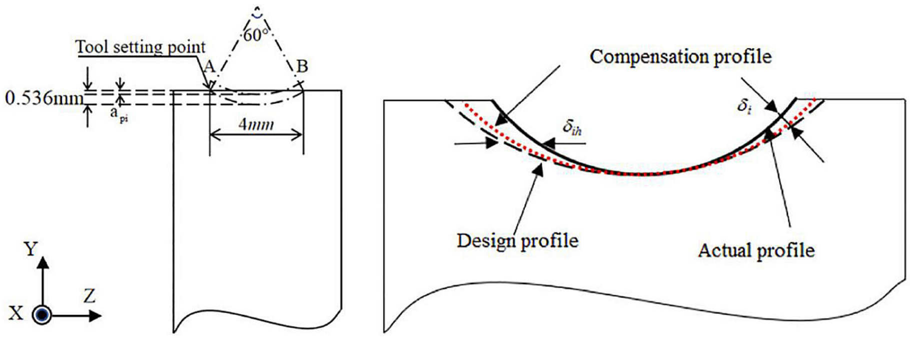

Figure 36. (a) Arc geometry, paths of laser beam, (b) error of arc-shape geometry, compensation path [44]

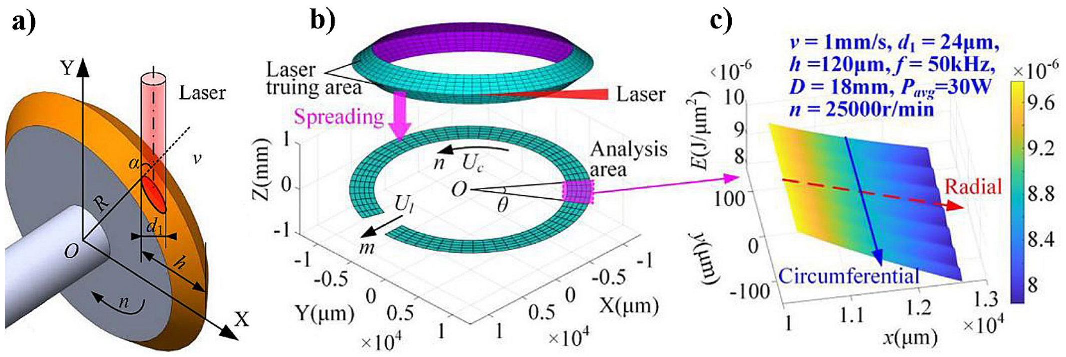

Figure 37. Energy modeling principle of V-shaped grinding wheel: (a) finite element mesh division of laser truing area, (b) analysis principle of laser energy density model [46]

was added to or subtracted from the Z coordinate of the laser path. Ablation was performed along the new path, followed by measurement to assess the accuracy of the resulting profile. This laser path compensation sequence was repeated until acceptable profile accuracy was achieved. In the described case, final profile accuracy was achieved after the third iteration. The final profile errors were: a radius error of 11.2 µm and a contour roundness error of 22.8 µm.

Distribution of laser beam energy density on the surface of a profile grinding wheel

The research results concerning the conditions for maintaining constant laser radiation energy density on the shaped grinding wheel surface during dressing are presented in [46]. The energy density distribution on the V-shaped grinding wheel surface was analyzed depending on the profiling parameters. The variable parameters were grinding wheel rotational speed *n* and the radiation beam positioning depth relative to the grinding wheel *h* – Figure 37a. The analysis was performed using the finite element method. A 2-dimensional model was constructed, which was a projection of the conical abrasive surface onto a plane. The model surface was divided by a finite element mesh with a width of 0.5 µm (Figure 37b).

Assuming the values *v* (scanning feed rate), d_1 (focus diameter), *f* (pulse frequency), *D* (maximum grinding wheel diameter) and P_{avg} (average laser power) as constants, the energy density distribution on the abrasive surface was modelled as a function of rotational speed *n* at a constant *h* (beam setting depth) and as a function of *h* at a constant *n*. The results of simulations in which *h* was variable showed no effect of *h* on the energy density distribution on the grinding wheel surface. However, a significant effect of the change in speed *n* on the energy density distribution in the radial and circumferential directions was noted – Figure 38. The calculations were performed for rotational speeds ranging from 2500 to 30,000 rpm. When the speed was lower than 9000 rpm, the variability of energy density was noticeable in the radial direction, which is a consequence of the high feed speed *v* relative to the rotational movement of the grinding wheel (Figure 38a). In this case, the ablation tracks did not overlap, and there were zones of lower energy density between them. These zones disappeared as the rotational speed increased and the tracks began to overlap. The variability in the radial direction was now due to the decreasing overlap of the spots of successive pulses as the radius of the grinding wheel increased (which results from the increasing peripheral speed of the surface points further away from the axis of rotation). As a result of the decrease in the U_p overlap ratio value, the energy density decreased (Figure 38b). At the highest analysed speeds *n*, an increasing influence of the decreasing U_p index value on the energy density

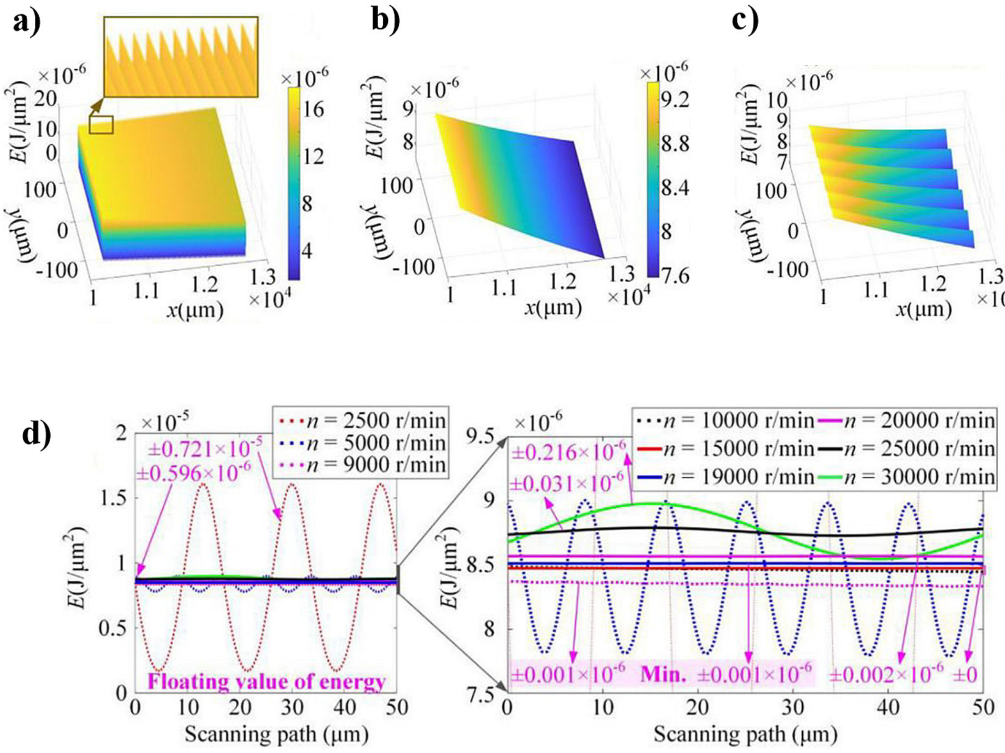

Figure 38. Influence of n on laser energy density distribution of V-shaped grinding wheel: (a) *n* = 2500 rpm, (b) *n* = 10,000 rpm, (c) *n* = 30,000 rpm, d) influence of n on radial and circumferential distribution of energy density (Note: radial direction is dotted line, circumferential direction is solid line) [46]

distribution can be observed. In addition to the change along the grinding wheel radius, there are changes in the distribution along the circumference of the grinding surface – the changes in energy density are wave-like (Figure 38c,d).

The theoretical considerations were verified experimentally by shaping a CBN grinding wheel with an electroplated bond (grain size 300 μm). In the tests, the power of the pulsed laser (P_{avg} 3–30 W, λ = 1064 nm, d = 24 μm, τ = 100 ns, f = 30 kHz) and the profiling time t were varied. The grinding wheel profile was assessed indirectly based on measurements of the surface profile of a graphite block ground with this grinding wheel.

According to the authors, the results of the study were consistent with the theoretical analysis. As the rotational speed of the grinding wheel n increased, the distance between the laser ablation marks on the surface of the grinding wheel decreased; at n = 30,000 rpm, they were no longer visible, and the surface roughness of the particles improved significantly. This indicated that the laser energy density was uniform at that moment. Increasing the profiling depth h, while leaving the other parameters at the same level, resulted in the removal of an increasingly larger layer of CBN particles, until their tops were levelled with the binder, which was unacceptable due to the abrasive properties of the tool. Measurements showed that profiling with an ablation depth of 30–50% of the grain size ensures the highest machining accuracy. Profiling tests with increasing power (18–30 W) confirmed the known regularity of increased ablation intensity of abrasive particles. Increasing power did not cause metamorphic changes in CBN grains, as is the case with diamond grains. The profiling time t played a particularly important role in obtaining an accurate outline of the grinding wheel tip. The lower energy density on the outer surface of the rotating grinding wheel limited the ablation intensity, which meant that to obtain the required angle and rounding of the profile top, it was necessary to repeat the scanning, thus extending the processing time. After 25 minutes of scanning with a depth of h = 150 μm, at n = 30,000 rpm and P_{avg} = 30 W, the geometry and protrusion of the grains above the binder were considered correct (Figure 39).

Table 2 summarizes the key properties of these methods, considering their advantages, limitations, and areas of application.

CONCLUSIONS

The presented review of laser dressing methods for profile grinding wheels indicates that the developed dressing techniques meet the requirements for profile accuracy, process efficiency, and wheel material integrity, particularly for diamond abrasives, to varying degrees. In classic tangential beam dressing, dressing efficiency depends primarily on maintaining the appropriate energy density at the irradiation site. Variations in the distance between the irradiated grinding wheel surface and the focal plane, resulting from topographic irregularities and profile shape, lead to beam defocusing and reduced ablation intensity. This phenomenon is particularly pronounced on steep slopes and curvilinear sections of the profile. Guiding the beam according to the nominal profile does not allow for faithful reproduction of these elements. Introducing a slight beam deflection in the tangential plane, which reduces the beam's angle of incidence on the side surfaces of the profile grinding wheel, reduces both defocusing and the beam's shadowing effect, resulting in higher accuracy of the resulting angle of inclination of these surfaces. However, this method is effective only within a limited range of deflection angle values. Too small a deflection does not reduce the inherent errors of this dressing method, while too large a deflection leads to excessive energy concentration and a decrease in the geometric accuracy of the profile.

The highest level of accuracy in profile geometry reproducing is achieved by compensation

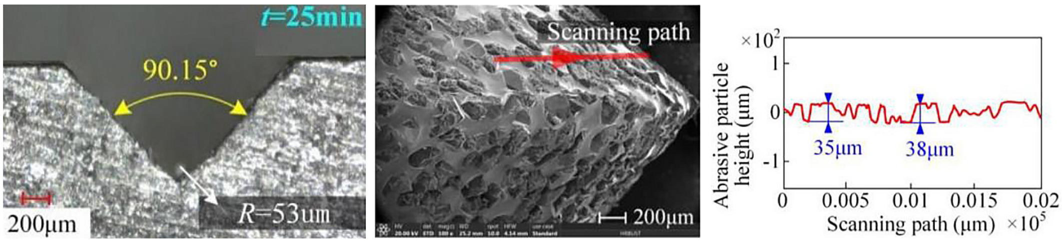

Figure 39. The profile and surface morphology of V-shaped grinding wheel after 25 min laser truing time [46]

Table 2. Comparison of laser dressing methods for profile grinding wheels

Method / Beam source	Principle of operation	Advantages	Limitations	Application
Tangential beam	Scanning along the generating grinding wheel with a fixed focus position	Versatility; ability to machining complex profiles	Sensitive to defocus and beam occlusion; limited accuracy in reproducing steep profile slopes and arcs	Standard grooves, shallow profiles
Deflected tangential beam	Slight beam deflection in the tangential plane	Minimizing the steep slope angle error of the profile	risk of over ablation with too much beam deflection	Profiles with steep slopes, angles close to 90°
Beam path modification by deviation compensation method	Beam path correction based on post-roughing measurement	Correction of local ablation errors; high profile accuracy	Precise measuring device; software synchronizing measurement results with control; greater control complexity	Precision grinding wheels of any profile
Segmented scanning method	Gradually shifting the focal plane to maintain the ablation threshold	Possibility of machining deep profiles; shortening the machining time	Need to know ablation threshold; greater control complexity	Machining of deep profiles from cylindrical blank, large differences in depth and angles
Nanosecond lasers	Thermal ablation	High efficiency of material removal	Risk of diamond graphitization, occurrence of heat-affected zone	Mainly CBN grinding wheels, roughing processes
Picosecond lasers	Ablation in the Coulomb regime	No graphitization of diamonds; minimal thermal effects	Lower efficiency; high source cost	Precise finishing diamond grinding wheels
Combined radial+tangential	Radial beam rough shaping + tangential beam finishing	High speed of shaping; high precision of finishing	Precise measuring device; software synchronizing measurement results with the control; measurement and processing on two separate devices	Machining deep profiles from cylindrical blank

methods, which rely on iterative correction of the beam path based on contour measurement after roughing. These methods enable deviations of the order of a few micrometers, which results from the ability to locally adapt the machining path to actual ablation conditions. However, this requires the use of high-resolution measurement systems and programs for determining the deviations between the actual and designed profiles and integrating these results with the machining machine control programs. This increases the duration of the entire process, especially when using measurement devices not integrated with the machining machines.

In the case of deep profiles created from cylindrical blanks, the primary problem is the gradual loss of ablation capacity associated with increasing distance between the designed machining point and the beam focus. The proposed segmented scanning method allows for maintaining similar ablation conditions by periodically changing the position of the beam focal plane relative to the grinding wheel surface. This approach avoids process dead zones and reduces machining time compared to conventional strategies, but requires knowledge of the grinding wheel's material ablation threshold. The offset distance can be determined computationally or based on an ongoing assessment of ablation intensity. The accuracy of plasma spectroscopy used for this purpose, due to its inertia, has proven to be limited.

The laser beam source has a significant impact on the achieved profile accuracy and material integrity of the grinding wheel. Nanosecond lasers, widely used in industry, provide high material removal rates but induce significant thermal stresses leading to degradation of grinding wheel material, a specially to diamond graphitization. Picosecond lasers, where ablation is governed by electrostatic phenomena, do not observe a heat-affected zone or graphitization, significantly improving surface quality and the stability of the abrasive layer properties. However, lower efficiency and higher equipment costs naturally limit their use in processes with high performance requirements.

REFERENCES

1. Guo Y., Yin Z. On-machine precision truing and error compensation of cup-shaped diamond grinding wheels with arc-shaped cutting edge. Micromachines. 2025; 16(9): 1050. https://doi.org/10.3390/mi16091050
2. Young H.T., Chen D.J. Online dressing of profile grinding wheels. Int. J. Adv. Manuf. Technol. 2006; 27: 883–888. https://doi.org/10.1007/s00170-004-2271-8
3. Ohmori H., Katahira K., Naruse T., Uehara Y., Nakao A., Mizutani M. Microscopic grinding effects on fabrication of ultra-fine micro tools. CIRP Ann. – Manuf. Techn. 2007; 56(1): 569–72. https://doi.org/10.1016/j.cirp.2007.05.136
4. Qian J., Ohmori H., Lin W.M. Internal mirror grinding with a metal/metal-resin bonded abrasive wheel. International Journal of Machine Tools & Manufacture 2001; 41(2): 193–208. https://doi.org/10.1016/S0890-6955(00)00067-5
5. Gołąbczak, M., Gołąbczak A., Tomczyk B. Electrochemical and x-ray examinations of erosion products during dressing of superhard grinding wheels using alternating current and ecological electrolytes of low concentration of chemical compounds. Materials 2021; 14: 1375. https://doi.org/10.3390/ma14061375
6. Gaoa B., Jina T., Qua M., Shanga Z., Tanga L. Electrochemical cleaning grinding (ECCG) of aluminum alloy 6061 with electroconductive resin-bonded diamond wheels. Journal of Manufacturing Processes 2020; 57: 806–816. https://doi.org/10.1016/j.jmapro.2020.07.041
7. Zhou D., Qiu Z. Metal-bonded diamond grinding wheel topography generated with electrical discharge dressing (EDD). Nanotechnology and Precision Engineering 2017; 15(4): 254–60. https://doi.org/10.13494/j.npe.20160081
8. Uhlmann E., Yabroudi S., Zimmermann S., Gerlitzky G., Polte M., Klink U., Sihling B. Electrical discharge dressing of honing stones. Precision Engineering 2020; 62: 151–161.
9. https://doi.org/10.1016/j.precisioneng.2019.11.020
10. Weingeartner E., Jaumann S., Kuster F., Boccadoro M. Special wire guide for on-machine wire electrical discharge dressing of metal bonded grinding wheels. Annals of the CIRP 2010; 59(1): 227–230. https://doi.org/10.1016/j.cirp.2010.03.010
11. Quanpeng He, Jin Xie, Kuo Lu, Hao Yang. Study on in-air electro-contact discharge (ECD) truncating of coarse diamond grinding wheel for the dry smooth grinding of hardened steel. Journal of Materials Processing Tech. 2020; 276: 116402. https://doi.org/10.1016/j.jmatprotec.2019.116402
12. Mizuno M., Karibe A., Yoshihara N., Nishikawa N., Iyama T. Development of a new truing device based on electro-contact discharge machining for metal bond grinding wheels. Materials Science Forum 2016; 874: 268–71. https://doi.org/10.4028/www.scientific.net/MSF.874.268
13. Guo B., Zhao Q. On-machine dry electric discharge truing of diamond wheels for micro-structured surfaces grinding. Int. J. Mach. Tool. Manu. 2015; 88: 62–70. http://dx.doi.org/10.1016/j.ijmachtools.2014.09.011
14. Dai L., Chen G., Li M., Yuan S. Experimental study on dressing concave trapezoidal diamond grinding wheel by electrical discharge grinding method. Diamond & Related Materials 2022; 128: 109218. https://doi.org/10.1016/j.diamond.2022.109218
15. Hirao M., Izawa M., Iguchi M. Waterjet in-process dressing (1st report). International Journal of the Japan Society for Precision Engineering 1998; 64(9): 1335–9. https://doi.org/10.2493/jjspe.64.1335
16. Axinte D.A., Stepanian J.P., Kong M.C., McGourlay J. Abrasive waterjet turning-An efficient method to profile and dress grinding wheels. Int. J. Mach. Tool. Manu. 2009; 49(3–4): 351–6. https://doi.org/10.1016/j.ijmachtools.2008.11.006
17. Zhang Z., Yao P., Zhang Z., Xue D., Wang C., Huang C., Zhu H. A novel technique for dressing metal-bonded diamond grinding wheel with abrasive waterjet and touch truing. Int. J. Adv. Manuf. Technol. 2017; 93: 3063–3073. https://doi.org/10.1007/s00170-017-0738-7
18. Wang Y., Zhou X.J., Hu D.J. An experimental investigation of dry-electrical discharge assisted truing and dressing of metal bonded diamond wheel. Int. J. Mach. Tool. Manu. 2006; 46(3–4): 333–42. https://doi.org/10.1016/j.ijmachtools.2005.05.022
19. Wegener K., Hoffmeister H.-W., Karpuschewski B., Kuster F., Hahmann W.-C., Rabiey M. Conditioning and monitoring of grinding wheels. CIRP Annals - Manufacturing Technology 2011; 60: 757–777. https://doi.org/10.1016/j.cirp.2011.05.003
20. Azarhoushang B., Zahedi A. Laser conditioning and structuring of grinding tools – A review. Adv. Manuf. 2017; 5: 35–49. https://doi.org/10.1007/s40436-016-0167-0
21. Deng H., Xu Z. Dressing methods of superabrasive grinding wheels: A review. Journal of Manufacturing Processes 2019; 45: 46–69. https://doi.org/10.1016/j.jmapro.2019.06.020
22. Cai S., Liu W., Song J., Deng K., Tang Y. Research and progress on truing and sharpening process of diamond abrasive grinding tools. Applied Sciences 2022; 12: 4683. https://doi.org/10.3390/app12094683
23. Jackson M.J., Khangar A., Chen X., Robinson G.M., Venkatesh V.C., Dahotre N.B. Laser cleaning and dressing of vitrified grinding wheels. Journal of Materials Processing Technology 2007; 185: 17–23. http://dx.doi.org/10.1016/j.jmatprotec.2006.03.109
24. Deng H., Chen G., He J., Zhou C., Du H., Wang Y. Online, efficient and precision laser profiling of

bronze-bonded diamond grinding wheels based on a single-layer deep-cutting intermittent feeding method. Optics & Laser Technology 2016; 80: 41–50. http://dx.doi.org/10.1016/j.optlastec.2015.12.021

25. Wei Zhou, Genyu Chen, Huajun Pan, Fengrong Luo, Yi Wei, Mingquan Li. Laser deflection tangential dressing complex-concave surface bronze-bonded diamond wheels. The International Journal of Advanced Manufacturing Technology 2022; 121: 5109–5123. https://doi.org/10.1007/s00170-022-09647-6
26. Wang X.Y., Wu Y.B., Wang J., Xu W.J., Kato M. Absorbed energy in laser truing of a small vitrified CBN grinding wheel. Journal of Materials Processing Technology 2005; 164–165: 1128–1133. http://dx.doi.org/10.1016/j.jmatprotec.2005.02.108
27. Tao N., Chen G., Liu Z., Luo F., Wei Y., Zhou W. Laser dressing of fine-grained metal-bonded diamond grinding wheels with concave surface. Optics & Laser Technology 2024; 175: 110812. https://doi.org/10.1016/j.optlastec.2024.110812
28. Bing Guo, Qingliang Zhao, Xin Yu. Surface microstructuring of coarse-grained diamond wheels by nanosecond pulsed laser for improving grinding performance. International Journal of Precision Engineering and Manufacturing 2014; 15(10): 2025–2030. https://doi.org/10.1007/s12541-014-0559-7
29. Xie K.G., Rushworth A., Chen H., Zhang X.Y., Huang Z.P., Shen Y.X. Generating precise non-flat grinding wheel surfaces via CO_2 laser ablation: Understanding the relationship between overlap rate and feed rate on composite materials. Journal of Manufacturing Processes 2022; 83: 339–353. https://doi.org/10.1016/j.jmapro.2022.09.008
30. Zhou W., Chen G., Pan H., Cao K., Luo F., Wei Y., Li M. Dual-laser dressing concave rectangular bronze-bonded diamond grinding wheels. Diamond & Related Materials 2022; 123: 108830. https://doi.org/10.1016/j.diamond.2022.108830
31. Zaitsev A.V., Kovalev O.B., Orishich A.M., Fomin V.M. Numerical analysis of the effect of the TEM00 radiation mode polarisation on the cut shape in laser cutting of thick metal sheets. Quantum Electronics 2005; 35(2): 200–204. https://doi.org/10.1070/QE2005v035n02ABEH002728
32. Dahotre, N.B., Harimkar S. Laser Fabrication and Machining of Materials. Berlin: Springer, 2008.
33. Gamaly E. G., Rode A. V., Tikhonchuk V. T., Luther-Davies B. Ablation of solids by femtosecond lasers: ablation mechanism and ablation thresholds for metals and dielectrics. Physics of Plasmas 2002; 9(3): 949–957. http://dx.doi.org/10.1063/1.1447555
34. Chen G., Cai S., Zhou C. On the laser-driven integrated dressing and truing of bronze-bonded grinding wheels. Diamond & Related Materials 2015; 60: 99–110. http://dx.doi.org/10.1016/j.diamond.2015.10.018
35. Orlandinia A., Baraldoa S., Portaa M., Valentea A. Ablation threshold estimation for femtosecond pulsed laser machining of AISI 316L. 55th CIRP Conference on Manufacturing Systems. Procedia CIRP 2022; 107: 617–622. http://dx.doi.org/10.1016/j.procir.2022.05.035
36. Chichkov B.N., Momma C., Nolte S., von Alvensleben F., Tunnermann A. Femtosecond, picosecond and nanosecond laser ablation of solids. Appl. Phys. 1996; A 63: 109–115. https://doi.org/10.1007/BF01567637
37. Dai L., Chen G., Li M., Yuan S. Efficient and precision dressing of arc-shaped diamond grinding wheel by laser dressing and electrical discharge dressing. Diamond & Related Materials 2022; 125: 108978. https://doi.org/10.1016/j.diamond.2022.108978
38. Deng H., Deng Z., Li S. Study on methods to optimize laser-sharpening quality, efficiency and topography. Precision Engineering 2016; 46: 409–416. http://dx.doi.org/10.1016/j.precisioneng.2016.05.005
39. Zhou W., Chen G., Pan H., Luo F., Wei Y., Li M. Laser precision profiling of small-angle bevel-edge contour grinding wheels. Journal of Materials Processing Tech. 2022; 305: 117591. https://doi.org/10.1016/j.jmatprotec.2022.117591
40. Walter C., Rabiey M., Warhanek M., Jochum N., Wegener K. Dressing and truing of hybrid bonded CBN grinding tools using a short-pulsed fibre laser. CIRP Annals - Manufacturing Technology 2012; 61: 279–282. http://dx.doi.org/10.1016/j.cirp.2012.03.001
41. Deng H., Xu Z. Laser dressing of arc-shaped resin-bonded diamond grinding wheels. Journal of Materials Processing Tech. 2021; 288: 116884. https://doi.org/10.1016/j.jmatprotec.2020.116884
42. Chen G., Deng H., Zhou X., Zhou C., He J., Cai S. Online tangential laser profiling of coarse-grained bronze-bonded diamond wheels. Int. J. Adv. Manuf. Technol. 2015; 79: 1477–1482. https://doi.org/10.1007/s00170-015-6963-z
43. Ackerl N., Warhanek M., Gysel J., Wegener K. Ultra-short pulsed laser conditioning of metallic-bonded diamond grinding tools. Materials and Design 2020; 189: 108530. https://doi.org/10.1016/j.matdes.2020.108530
44. Chen G., Wei Y., Peng Y.B., Wang Y. Fiber laser CNC tangential turing V-shaped concave diamond grinding wheel system based on machine vision technology. The International Journal of Advanced Manufacturing Technology 2019; 104: 4077–4090. https://doi.org/10.1007/s00170-019-04112-3
45. Zhou W., Chen G., Gao M., Wang Y., Wei Y., Li W. Laser machining and compensation truing of small concave-arc bronze-bonded diamond grinding wheels. Journal of Manufacturing Processes 2022; 79: 815–826. https://doi.org/10.1016/j.jmapro.2022.05.016
46. Deng H., He C., Liu W., Xiong W. Trajectory planning of deep-cutting laser profiling of superabrasive profile grinding wheels. Engineering Science and Technology, an International Journal 2023; 48: 101581. https://doi.org/10.1016/j.jestch.2023.101581